LIFE SCIENCES

Identification of human cranio-maxillofacial skeletal stem cells for mandibular development

Zhuo Wang[1,2]†, Kun Wang[3]†, Yejia Yu[1]†, Jing Fu[4,5]†, Siyuan Zhang[1], Maojiao Li[1,2], Jian Yang[1], Xuanhao Zhang[1,2], Xiaodong Liu[1,2], Fengqiong Lv[5,6], Li Ma[5,6], Haoyang Cai[3]*, Weidong Tian[1,2]*, Li Liao[1,2]*

Compared with long bone that arises from the mesoderm, the major portion of the maxillofacial bones and the front bone of the skull are derived from cranial neural crest cells and undergo intramembranous ossification. Human skeletal stem cells have been identified in embryonic and fetal long bones. Here, we describe a single-cell atlas of the human embryonic mandible and identify a population of cranio-maxillofacial skeletal stem cells (CMSSCs). These CMSSCs are marked by interferon-induced transmembrane protein 5 (IFITM5) and are specifically located around the periosteum of the jawbone and frontal bone. Additionally, these CMSSCs exhibit strong self-renewal and osteogenic differentiation capacities but lower chondrogenic differentiation potency, mediating intramembranous bone formation without cartilage formation. IFITM5$^+$ cells are also observed in the adult jawbone and exhibit functions similar to those of embryonic CMSSCs. Thus, this study identifies CMSSCs that orchestrate the intramembranous ossification of cranio-maxillofacial bones, providing a deeper understanding of cranio-maxillofacial skeletal development and promising seed cells for bone repair.

INTRODUCTION

The reconstruction of cranio-maxillofacial bone defect is more challenging than that of the limb bone defect, owing to the need for both functional and esthetic recovery. Now, stem cell–guided regenerative medicine is the most promising therapeutic strategy for the reconstruction of cranio-maxillofacial bone defect. Thus, the identification of specific cranio-maxillofacial skeletal stem cells (CMSSCs) will enable the development of stem cell therapies for cranio-maxillofacial bone regeneration (*1*, *2*).

The skeletal tissue of vertebrates has different embryological origins. Axial bone (such as vertebrae) and appendicular bone (such as long bone) originate from the mesoderm (*3*–*5*), whereas the cranio-maxillofacial skeleton bones, including the maxilla, mandible, and frontal bone, are derived from cranial neural crest cells (CNCCs), which originate from a region of ectoderm at the border of the neural plate and nonneural ectoderm, and migrate from the neural tube into the pharyngeal arches (*6*–*8*). Moreover, the development process of the cranio-maxillofacial skeleton is distinct from that of the vertebrae and long bones. The vertebrae and long bones are ossified mainly through endochondral ossification, during which the condensed mesenchyme first develops into cartilaginous templates, and the surrounding mesenchyme subsequently invades the hypertrophic zone to become osteoblasts (*9*, *10*). In contrast, the craniofacial skeleton is formed mostly through intramembranous osteogenesis, during which skeletal stem cells (SSCs) directly differentiate into osteoblasts and synthesize bone matrix without chondrogenic differentiation (*11*–*13*). In skeleton development, it is unclear whether different SSCs are responsible for the development of the two distinct types of bones.

Previous studies based on genetic lineage–tracing model and flowcytometry sorting had identified Lin$^-$CD51$^+$Thy$^-$6C3$^-$CD105$^-$CD200$^+$ SSCs in the growth plate of mouse long bone (*14*). These SSCs gave rise to bone, cartilage, and stroma, but not fat, providing deeper insight into mouse SSCs' developmental hierarchy. Similarly, Lin$^-$PDPN$^+$CD146$^-$CD73$^+$CD164$^+$ SSCs of human long bone were isolated from the growth plate of a 17-week human fetal femur. These SSCs were capable of self-renewal and multilineage differentiation to bone, cartilage, and stroma (*15*). He *et al.* (*16*) mapped the single-cell atlas of human limb buds and embryonic long bone and identified embryonic perichondrial SSCs with the phenotype Lin$^-$PDGFRA$^{low/-}$PDPN$^+$CADM1$^+$. Perichondrial SSCs could generate the osteochondral lineage but not adipocytes or stroma. These findings highlight that the long bone is formed and maintained by unique SSCs (*17*).

However, the SSCs involved in the development of cranio-maxillofacial bone have not been identified. Upon grafting the mandibular periosteum into a tibial bony defect, the bony matrix directly bridged the defect. Meanwhile, the transplantation of tibial periosteum cells into mandibular injury sites resulted in the detection of cartilage instead of bone (*18*). These findings suggested that distinct SSCs with different potency existed in different embryonic origin. A previous single-cell RNA sequencing (scRNA-seq) study on calvaria demonstrated that CNCCs were directly converted into osteoprogenitors. Additionally, none of the calvarial subsets highly resembled perichondrial SSCs (*16*), suggesting the divergence of stem cell types between intramembranous and endochondral development.

Until now, several populations of SSCs in the mouse cranio-maxillofacial bone have been dissected (*19*). Krt14$^+$Ctsk$^+$ progenitors,

---

[1] State Key Laboratory of Oral Diseases and National Clinical Research Center for Oral Diseases and Engineering Research Center of Oral Translational Medicine, Ministry of Education and National Engineering Laboratory for Oral Regenerative Medicine, West China Hospital of Stomatology, Sichuan University, Chengdu 610041, People's Republic of China. [2] Department of Oral and Maxillofacial Surgery, West China Hospital of Stomatology, Sichuan University, Chengdu 610041, People's Republic of China. [3] Center of Growth, Metabolism and Aging, Key Laboratory of Bio-Resource and Eco-Environment of Ministry of Education, College of Life Sciences, Sichuan University, Chengdu, China. [4] Department of Reproductive Endocrinology, West China Second University Hospital, Sichuan University, Chengdu 610041, China. [5] Key Laboratory of Birth Defects and Related Diseases of Women and Children, Sichuan University, Ministry of Education, Chengdu 610041, China. [6] Department of Operating Room Nursing, West China Second University Hospital, Sichuan University, Chengdu, China.

*Corresponding author. Email: lliao@scu.edu.cn (L.L.); haoyang.cai@scu.edu.cn (H.C.); drtwd@sina.com (W.T.)

†These authors contributed equally to this work.

which were detected in the regenerated tissue after maxillary sinus floor lifting, served as osteoprogenitors in maxillofacial bone regeneration (*20*). Comparative analysis of mesenchymal cells from the jawbone periosteum and bone marrow revealed Ctsk^{+}Ly6a^{+} periosteal osteogenic progenitors that contributed to the repair of the bone defect (*21*). Comparative analysis of cell compositions between the alveolar bone and long bone revealed a Fat4^{+} cell population in the constantly remodeled alveolar bone (*22*). This cell population exhibited a strong osteogenic differentiation ability in vivo and in vitro. These findings indicated that adult SSCs of different origins were characterized by distinct biomarkers. Recently, Yuan *et al.* (*23*) used single-cell analysis to reveal a sequential series of cell fate decision-making processes of postmigratory CNCCs within the embryonic mouse mandibles and identified a population of *Gbx2*-labeled cells in the proximal domain that differentiated into multiple lineages. However, SSCs involved in human mandibular morphogenesis have not been identified. Elucidation of the lineage hierarchy of CNCCs and identification of SSCs of the human cranio-maxillofacial skeleton will improve our understanding of cranio-maxillofacial bone development and enable the development of SSC-based therapies for skeletal regeneration.

In this study, the human embryonic mandible was subjected to scRNA-seq to capture various developing stages of cell types and determine their differentiation trajectories, which consequently provided a comprehensive view of human mandible development. By applying a standardized method of projecting laser capture microdissection sequencing (LCM-seq) data into scRNA-seq data, we identified an interferon-induced transmembrane protein 5 (IFITM5)$^{+}$ CMSSCs, with strong capacity of self-renewal and osteogenic differentiation but poor chondrogenic differentiation capacity. Unlike other IFITM proteins that were broadly expressed, IFITM5 was previously identified as an osteogenesis-specific membrane protein and involved in bone mineralization (*24*). Mutations in the *IFITM5* gene have been linked to osteogenesis imperfecta type V and disrupt early skeletal homeostasis, in part, by activating extracellular signal–regulated kinase signaling and downstream SOX9 protein (*25*). Different sites and cross-species comparisons revealed that CMSSCs were involved in the early intramembranous osteogenesis of cranio-maxillofacial bone, offering a cellular basis for the differential bone formation modes between cranio-maxillofacial bone and long bone. Additionally, IFITM5^{+} bone marrow stromal cells (BMSCs) were detected in the adult human jawbone and exhibited strong bone regeneration and repair abilities. Thus, IFITM5^{+} BMSCs represent a potential cellular source for regenerative applications in bone defect. These findings indicate that IFITM5^{+} CMSSCs are involved in the development of human cranio-maxillofacial skeleton.

RESULTS

Integrated analyses of single-cell transcriptomes during human mandible development

To investigate the fate decisions of postmigratory CNCCs during human mandibular morphogenesis, human embryos mandibles were isolated at gestational week 8 (GW8), GW9, GW9.5, GW10, and GW11. During this period, the morphology of the mandibular skeleton was basically formed. The mandible samples were digested into single-cell suspension using a modified protocol. The transcriptomes of individual cells were analyzed with scRNA-seq (Fig. 1A). Cells from all samples were integrated and divided into 13 cell populations using unsupervised clustering and marker analysis (Fig. 1B and fig. S1, A and B): CNC-derived mesenchymal cells (*POSTN*$^{+}$ and *SFRP2*$^{+}$) for 11.3%, common progenitors (*OGN*$^{+}$ and *FOXP2*$^{+}$) for 20.1%, stromal cells (*CXCL14*$^{+}$ and *TWIST2*$^{+}$) for 21.2%, neuronal cells (*SPARCL1*$^{+}$ and *NR2F2*$^{+}$) for 9.5%, chondrogenic cells (*COL9A1*$^{+}$ and *ACAN*$^{+}$) for 13.9%, osteogenic cells (*RUNX2*$^{+}$ and *SP7*$^{+}$) for 2.0%, odontogenic cells (*LHX6*$^{+}$ and *PAX9*$^{+}$) for 6.1%, cycling cells (*HIST1H1A*$^{+}$ and *HIST1H1B*$^{+}$) for 1.9%, endothelial cells (*CLDN5*$^{+}$ and *CDH5*$^{+}$) for 2.4%, epithelial cells (*KRT17*$^{+}$ and *KRT13*$^{+}$) for 0.4%, immune cells (*PTPRC*$^{+}$ and *S100A9*$^{+}$) for 2.0%, myogenic cells (*MYLPF*$^{+}$ and *ACTC1*$^{+}$) for 7.6%, and glial cells (*PTPRZ1*$^{+}$ and *SOX10*$^{+}$) for 1.5%. The dot plot of signature genes in all subpopulations indicated the reliability of the clustering result (Fig. 1C). Pearson correlation analysis revealed that mesenchymal and non-mesenchymal cells clustered together respectively (fig. S1C).

To examine the dynamic multi-differentiation trajectory of CNCCs, mesenchymal cell clusters were circled and subjected to pseudotime analysis using Monocle 3 (Fig. 1D). The predicted trajectory suggested that the serial fate decision of CNC-derived mesenchymal cells differentiated into initial three directions, with one diverging toward neuronal lineage, one flowing toward stromal lineage, and one becoming common progenitors. Then, common progenitors further branched into three different lineages: the *RUNX2*$^{+}$ osteogenic lineage, *SOX9*$^{+}$ chondrogenic lineage, and *LHX6*$^{+}$ odontogenic lineage. Consistent with the pseudotime analysis results, the characteristic genes in CNC-derived mesenchymal cells (*POSTN* and *SFRP2*) were gradually down-regulated upon terminal differentiation, whereas those in neuronal lineage (*NRG1* and *NRCAM*), stromal lineage (*TWIST2* and *CXCL14*), chondrogenic lineage (*SOX9* and *COL2A1*), and osteogenic lineage (*RUNX2* and *MSX1*) were gradually up-regulated with differentiation toward different lineages (Fig. 1E). Gene ontology (GO) analysis also showed that common progenitors and osteogenic cells were enriched with genes involved in regulating ossification processes, while chondrogenic cells were enriched with genes involved in cartilage condensation, which supported the clustering results above (Fig. 1F).

Identification of cranio-maxillofacial SSCs through combination of scRNA-seq with LCM-seq

Unlike long-bone developmental process in which the cartilaginous templates are gradually replaced by the ossified bone tissue, the intermediate part of Meckel's cartilage (MC) in the mandible is dispensable for osteogenic process and undergoes apoptosis to become fibrous tissue. The primary ossification center composed of condensed CMSSCs is on the mesiobuccal side of MC and differentiates into osteoblasts to generate osteoid tissue (*11*, *12*). While scRNA-seq has already identified a subpopulation of osteogenic cells during mandible development, we tried to identify the CMSSCs in the ossification center within the single-cell atlas. To provide original spatial location information of the subpopulations identified by scRNA-seq, we performed LCM-seq (Fig. 2A). The condensed CMSSCs adhered closely to periosteum and the Meckel's chondrocytes (MCCs) at GW9 to GW12 human mandibles were isolated (Fig. 2B and fig. S2A), and a high-quality full-length transcriptome was generated from the LCM-dissected areas. Pearson correlation analysis show that CMSSCs1 to CMSSCs5 and MCCs1 to MCCs3 clustered separately (fig. S2B). Differentially expressed genes (DEGs) of CMSSCs and MCCs were analyzed and visualized using the

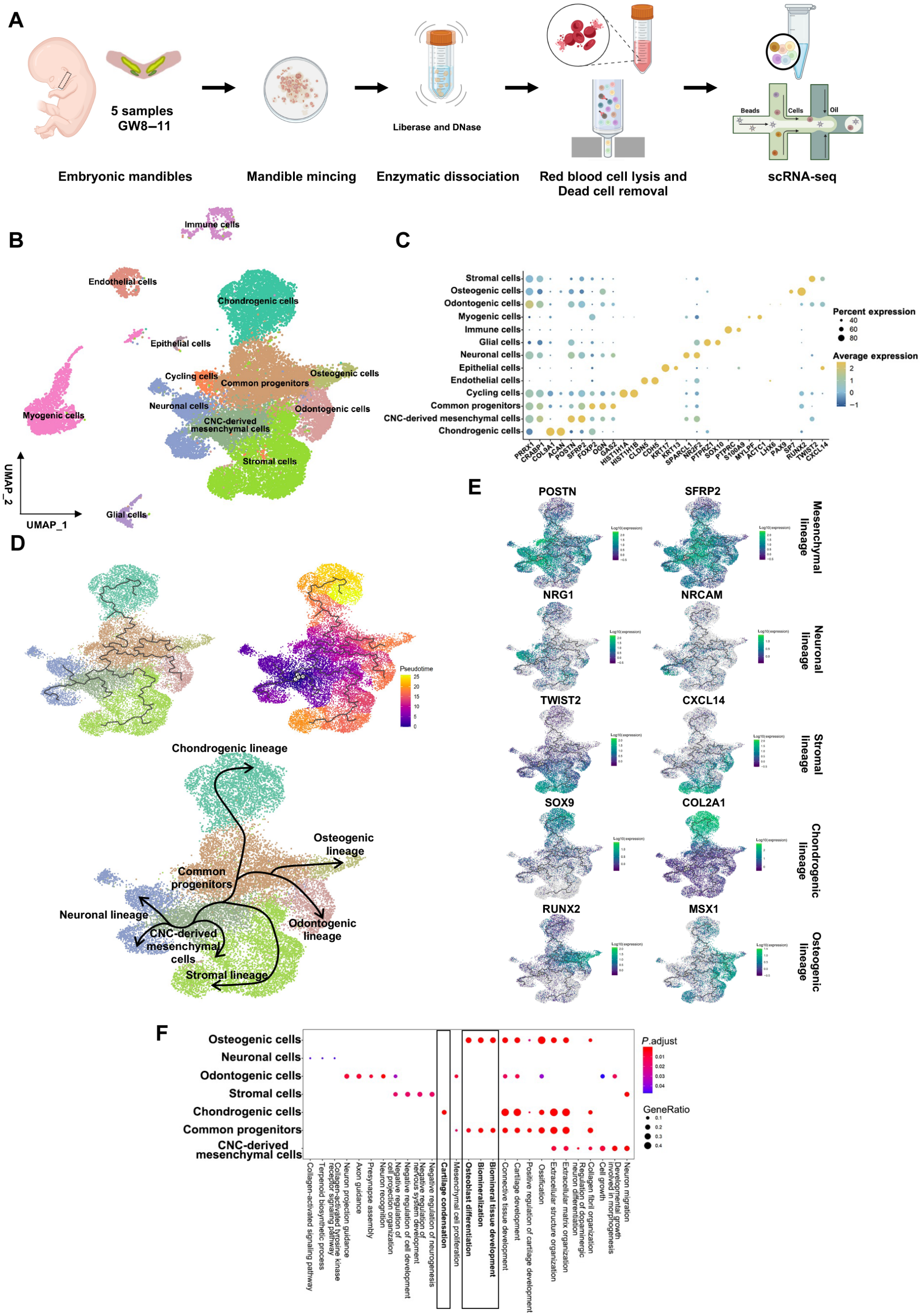

Fig. 1. Integrated cell atlas of human embryonic mandible. (**A**) Schematic illustration of the scRNA-seq workflow. Five human embryonic mandibles from GW8 to GW11 were processed for scRNA-seq. DNase, deoxyribonuclease. (**B**) Visualization of 13 subsets by integrated Uniform Manifold Approximation and Projection (UMAP) plots. (**C**) Dot plots showing the expression of individual feature genes in 13 subsets. (**D**) Developmental trajectory of CNC-derived mesenchymal cells inferred by Monocle 3. Top left: Pseudotime trajectory colored by clusters. Top right: Pseudotime trajectory colored by timeline. Bottom: Schematic diagram of the predictable differentiation trajectory. (**E**) Expression of selected differentially expressed marker genes for each cell lineage in green. (**F**) GO functional analysis of differentially expressed genes (DEGs) in the mesenchymal subsets.

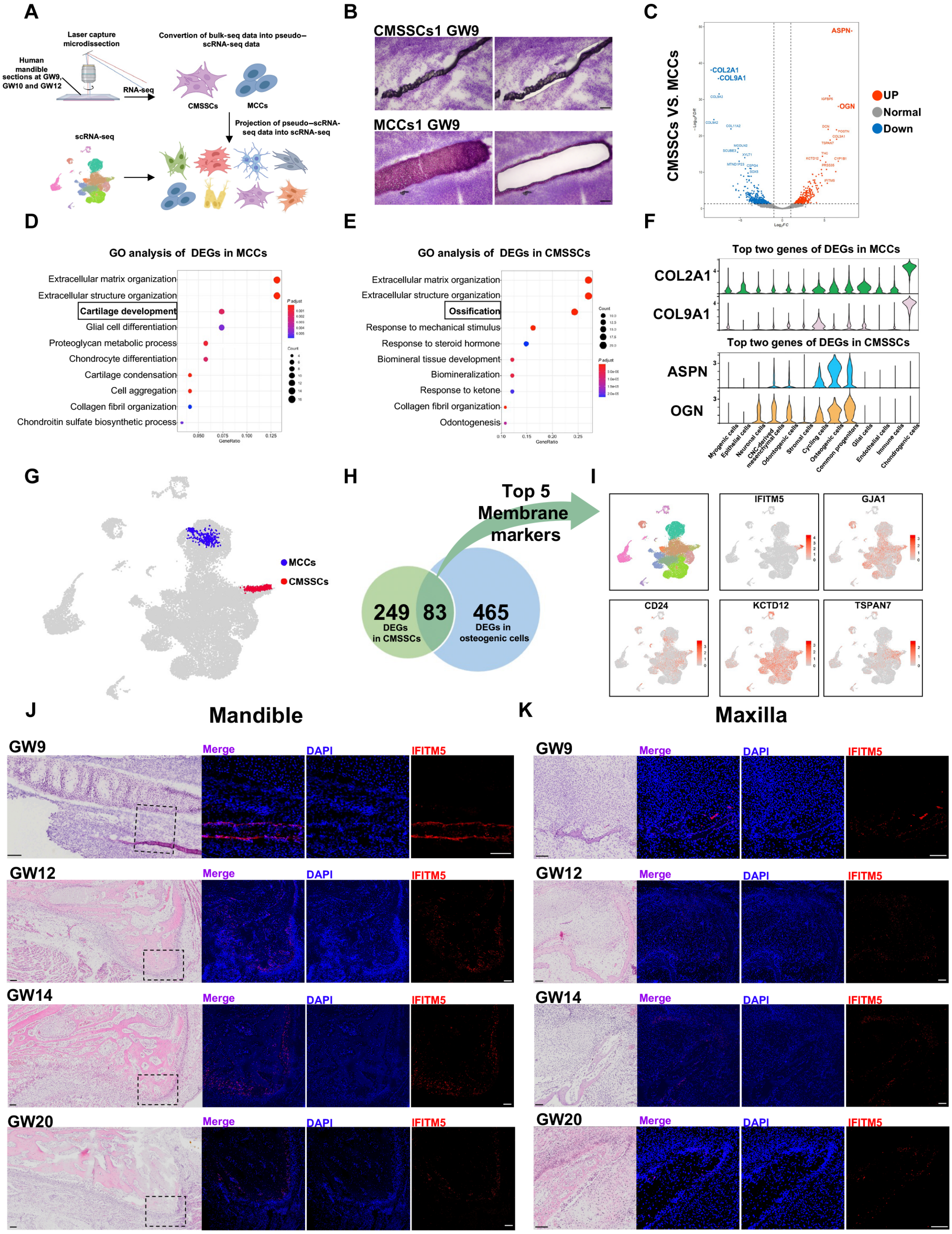

Fig. 2. Characterization of the CMSSCs in human embryonic mandible and identification of IFITM5 as a phenotypic marker of CMSSCs. (**A**) Schematic drawing of the combined scRNA-seq and LCM-seq. (**B**) Representative images showing the areas of CMSSCs1 and MCCs1 collected by LCM from GW9 mandible sections. Scale bars, 100 μm. (**C**) Volcano plot exhibiting DEGs distribution between CMSSCs and MCCs, and the top two DEGs in CMSSCs (*ASPN* and *OGN*) and MCCs (*COL2A1* and *COL9A1*) labeled, respectively. (**D**) GO analysis of DEGs in MCCs showing the top 10 terms ranked by enrichment score. (**E**) GO analysis of DEGs in CMSSCs showing the top 10 terms ranked by enrichment score. (**F**) Violin plots showing the expression level of *COL2A1*, *COL9A1*, *ASPN*, and *OGN* in the clusters of scRNA-seq data. (**G**) Projection of pseudo–single-cell data processed by LCM-seq data of CMSSCs and MCCs into the scRNA-seq data. (**H**) Venn diagram illustrating the numbers of DEGs in CMSSCs and osteogenic cells and the numbers of intersections. (**I**) UMAP distribution of top five membrane markers among intersection genes. (**J**) Hematoxylin and eosin (H&E) staining of GW9, GW12, GW14, and GW20 mandible sections. Immunofluorescence staining for IFITM5 performed on the areas marked with black dashed lines. Scale bars, 100 μm. (**K**) H&E staining of GW9, GW12, GW14, and GW20 maxilla sections. Immunofluorescence staining for IFITM5 performed on the areas marked with black dashed lines. Scale bars, 100 μm.

volcano plot (Fig. 2C). GO analysis revealed that DEGs in MCCs and CMSSCs were involved in cartilage development and ossification, respectively (Fig. 2, D and E). Of these, the top two genes of DEGs in MCCs, *COL2A1* and *COL9A1*, were notably expressed in chondrogenic cells, and the top two genes of DEGs in CMSSCs, *ASPN* and *OGN*, were highly expressed in osteogenic cells and common progenitors (Fig. 2F). The results of LCM-seq were consistent with those of scRNA-seq, suggesting the reliability of LCM-seq results. To clarify the distribution of CMSSCs in the scRNA-seq atlas, the LCM-seq data were transformed into a sparse matrix as pseudo–single-cell data and then projected into scRNA-seq using the R package project LSI according to the Granja's method (*26*). The merged dataset showed that CMSSCs1 to CMSSCs5 highly coincided with osteogenic cells, and that MCCs1 to MCCs3 were completely projected into chondrogenic cells (Fig. 2G and fig. S2C), indicating that the projection approach was reliable. To verify the above projection results, the method of Roels *et al.* (*27*) was used to directly mapped LCM-seq data onto the single-cell atlas. This approach demonstrated that CMSSCs1 to CMSSCs5 were entirely integrated with the osteogenic lineage (fig. S2D), indicating that CMSSCs were osteogenic lineage cells.

To search the specific surface markers of CMSSCs, the DEGs in CMSSCs (249 genes, from LCM-seq) and DEGs in osteogenic cells (465 genes, from scRNA-seq) were intersected to obtain 83 overlapping genes that comprised 17 genes encoding membrane protein (Fig. 2H). These 17 genes were ranked according to the order of DEGs in osteogenic cells. The top five genes were selected and depicted in the Uniform Manifold Approximation and Projection (UMAP) plot (Fig. 2I). Of these, *IFITM5* was specifically and differentially expressed in CMSSCs. Moreover, UMAP plots showed that the *IFITM5*$^+$ cells were not detectable at GW8 but appeared at GW9 and persisted until GW11, indicating that these cells were involved in early mandible bone formation (fig. S2E). Subsequently, the spatial distribution of IFITM5$^+$ CMSSCs was explored. Immunofluorescence staining of GW9 mandible showed that IFITM5$^+$ cells adhered tightly to the membrane of the bone matrix and were not detected on the MC (Fig. 2J and fig. S2F). In the GW12 mandible, hematoxylin and eosin (H&E) staining revealed that MC still existed and surrounded by the mineralized bone. Immunofluorescence staining showed that IFITM5 was specifically expressed in the endosteum but not in the mineralized bone tissue and MC (Fig. 2J and fig. S2F). In the GW14 mandible, H&E staining displayed that the intermediate portion of the MC underwent hypertrophy and degradation. Likewise, the IFITM5$^+$ cells were localized in the endosteum but not in the MC (Fig. 2J and fig. S2F). In the GW20 mandible, the MC was completely degraded and IFITM5$^+$ cells still resided in the endosteum (Fig. 2J). Analysis of the percentage of IFITM5$^+$ cells in periosteal cells showed no difference between GW12 and GW14 but decreased markedly at GW20 (fig. S2G). Meanwhile, IFITM5 was also detected in the maxillary periosteal surface in the GW9, GW12, GW14, and GW20 (Fig. 2K).

The spatial relationship between IFITM5 and known markers in human mandible

To determine the spatial relationship of IFITM5 with other known markers, IFITM5 with proliferation marker (Ki67), SSC markers (Ctsk, Gli1, and Gremlin1) (*28*–*30*), mesenchymal cell makers (Prrx1 and Dlx5) (*23*), and osteogenic marker (RUNX2) were co-stained in GW9 and GW10 mandibles (Fig. 3, A and B). Immunofluorescent staining revealed that numerous IFITM5$^+$ cells were co-expressed with Ki67, indicating their active proliferative state. IFITM5$^+$ population was specifically expressed around the periosteum and strongly co-expressed typical SSC markers (Ctsk, Gli1, and Gremlin1) and mesenchymal cell makers (Prrx1 and Dlx5). In addition, RUNX2$^+$ cells in the bone matrix were not labeled by the IFITM5.

Compared with the Ctsk$^+$ cells, IFITM5$^+$ cells were more specifically localized to the endosteum (Fig. 3C). Analysis of the colocalization demonstrated that 95.87 ± 2.23% of IFITM5$^+$ cells expressed Ctsk in GW12 mandible, and 94.26 ± 2.2% of IFITM5$^+$ cells expressed Ctsk in GW14 mandible (Fig. 3D), showing that nearly all IFITM5$^+$ cells were also Ctsk-positive. In addition, the IFITM5 hardly co-stained with osteoblast marker osteopontin (OPN), suggesting that IFITM5 marked a group of SSCs rather than mature osteoblasts (Fig. 3E). Collectively, these fluorescence results implied that IFITM5 could be a specific surface marker for labeling CMSSCs in human embryonic mandible.

IFITM5$^+$ CMSSCs were tissue specific during early intramembranous ossification

The cellular lineages (common progenitors, osteogenic cells, and chondrogenic cells) of human embryonic mandibles were integrated with mesenchymal cells of other bone tissues using data from previous studies (fig. S3, A to D) (*16*, *23*, *31*). The *IFITM5*$^+$ subset was identified in the 8-week-postconception (WPC) human calvaria and exhibited gene expression profiles (*DLX5*, *RUNX2*, and *IFITM5*) similar to those of CMSSCs (Fig. 4A). However, the *IFITM5*$^+$ subset was barely detected in the 8-WPC human long bone (Fig. 4B and fig. S4A) and GW9 human vertebra (Fig. 4C). In addition, the CMSSCs were found in the mouse mandibles at embryonic day 12.5 (E12.5) and E14.5 but scarcely at E10.5 (Fig. 4D and fig. S4B). Likewise, *IFITM5* expression emerged later during human mandible development, as it was not detected at GW8 (fig. S4C). This suggested that *IFITM5*$^+$ CMSSCs were involved in mandible bone formation, and the development pattern was conservative across species. The distribution of chondrogenic-associated genes (*SOX9* and *COL2A1*) in the integrated dataset (fig. S4, D to G) indicated that the integrated data could effectively distinguish different lineages. Consistently, immunofluorescence analysis showed that the IFITM5$^+$ cells could be observed in the periosteum of the GW9 human frontal bone (Fig. 4E), which were distinct from Gli1$^+$ cells distributed throughout the periosteum, dura, and sutures of calvaria during the early stage of postnatal development (*29*). IFITM5$^+$ cells were not detectable in the perichondrium of the GW9 human long bone and vertebra (Fig. 4, F and G), indicating that the CMSSCs were distinct from the Ctsk$^+$ cells identified in the long bone (*28*). The IFITM5$^+$ cells became detectable in the periosteum of the E16.5 mouse mandible at protein level, but not in the E14.5 (Fig. 4H), suggesting that gene expression at the protein level was later than that of transcript level. Together, these results indicated that IFITM5$^+$ cells contributed to the intramembranous ossification of cranio-maxillofacial bone.

CMSSCs exhibited greater proliferation and mineralization capacity but lower chondrogenic differentiation

Next, IFITM5$^+$ cells were isolated from embryonic mandibles for stem cell characterization. IFITM5$^+$ cells accounted for 4.26% of the embryonic mandibles. IFITM5$^+$ cells were isolated using flow cytometry with a gating strategy for Zombie$^-$ (used to exclude dead

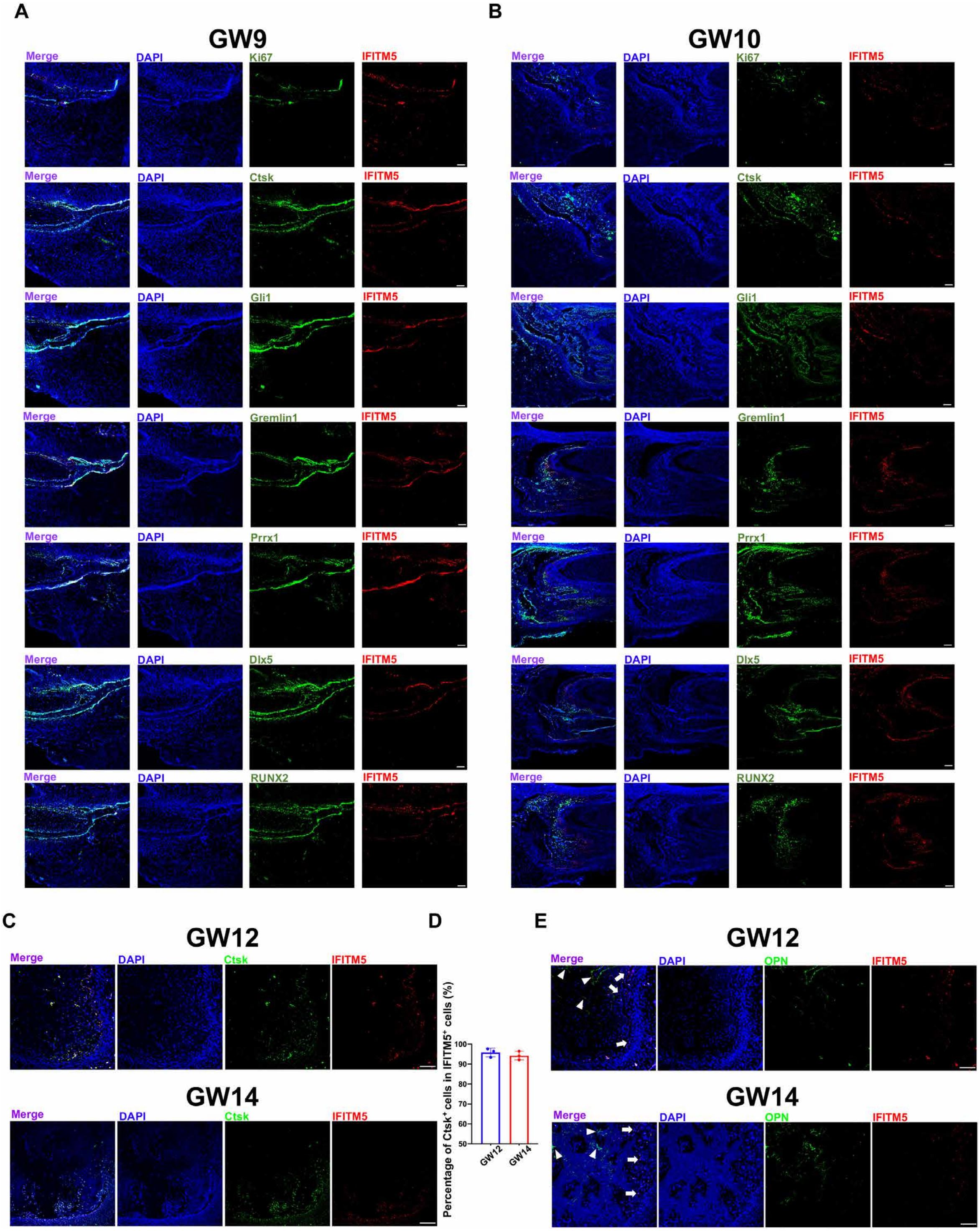

Fig. 3. Immunofluorescent colocalization of IFITM5 with other known markers. (**A**) Immunofluorescence double staining of Ki67, Ctsk, Gli1, Gremlin1, Prrx1, Dlx5, and RUNX2 (green) with IFITM5 (red) in GW9 mandible. Scale bars, 100 μm. (**B**) Immunofluorescence double staining of Ki67, Ctsk, Gli1, Gremlin1, Prrx1, Dlx5, and RUNX2 (green) with IFITM5 (red) in GW10 mandible. Scale bars, 100 μm. (**C**) Immunofluorescence double staining of Ctsk (green) with IFITM5 (red) in GW12 and GW14 mandibles. Scale bars, 100 μm. (**D**) Percentage of IFITM5$^+$ cells in Ctsk$^+$ cells in GW12 and GW14 mandibles (*n* = 3). (**E**) Immunofluorescence double staining of OPN (green) with IFITM5 (red) in GW12 and GW14 mandibles. White arrows indicated IFITM5$^+$ cells, and white triangular arrows indicated OPN$^+$ osteoblasts. Scale bars, 100 μm.

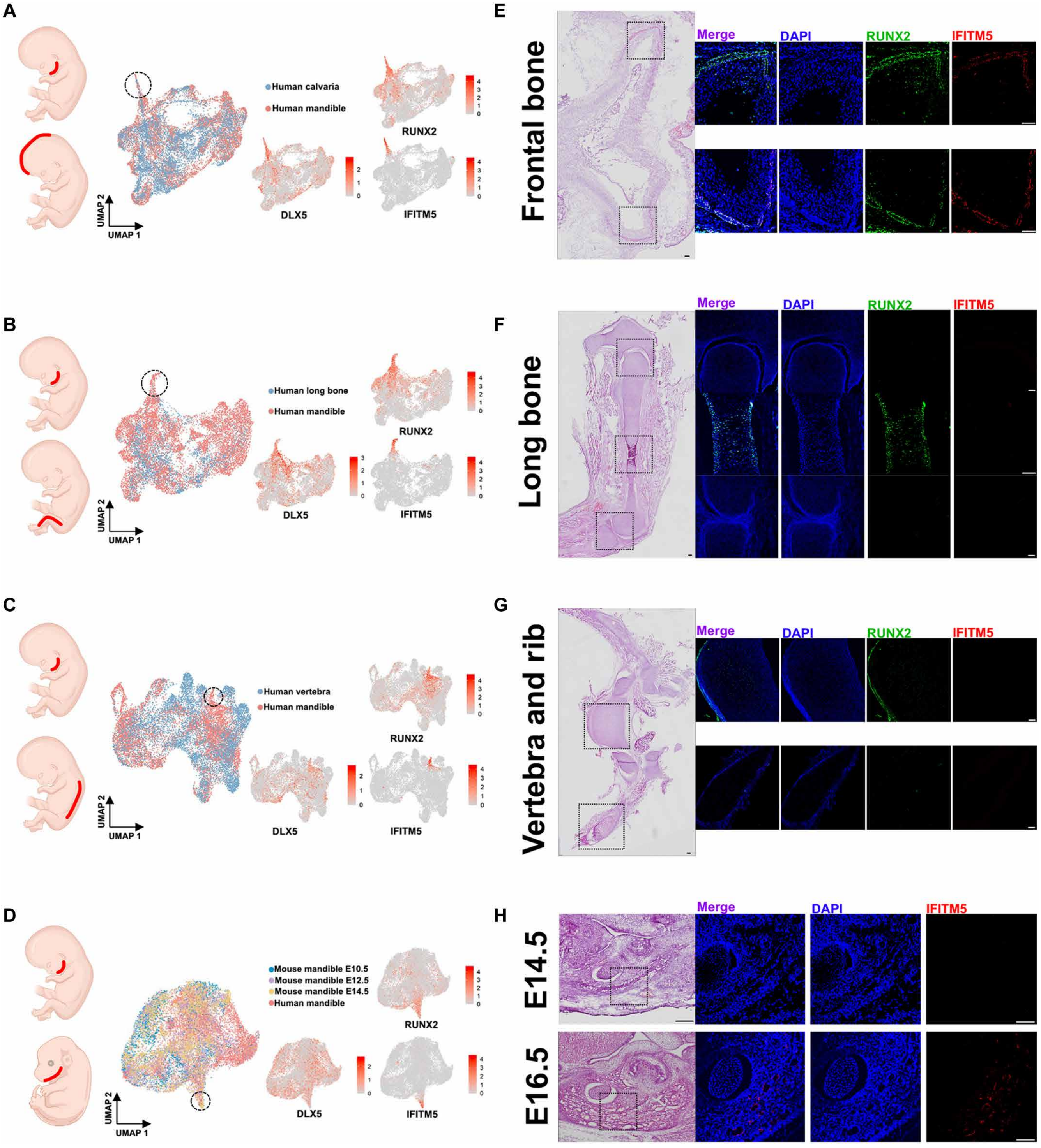

Fig. 4. Different sites and cross-species comparisons of CMSSCs. UMAP atlas of integrated analysis from cellular lineages (common progenitors, osteogenic cells, and chondrogenic cells) of human embryonic mandibles and mesenchymal cells of (**A**) human 8-WPC calvaria, (**B**) human 8-WPC long bone, (**C**) human GW9 vertebra, and (**D**) mouse E10.5 to E14.5 mandibles. CMSSC-like cells were circled with a dashed line and feature plots to the right visualize expression of *DLX5*, *RUNX2*, and *IFITM5*. H&E staining of (**E**) human GW9 calvaria, (**F**) human GW9 long bone, (**G**) human GW9 vertebra, and (**H**) mouse E14.5 and E16.5 mandibles. Immunofluorescence staining of RUNX2 or IFITM5 of the area in the dotted box. Scale bars, 100 μm.

cells) CD31$^-$CD45$^-$CD235ab$^-$ (used to exclude endothelial and hematopoietic cells) and IFITM5$^+$ (Fig. 5, A and B). The IFITM5$^+$ and IFITM5$^-$ cells were of typical shape of mesenchymal stroma cells when cultured in vitro and showed the high expression of CD90, CD105, and CD44 but lack of expression of CD34, CD45, and CD11b (fig. S5, A and B). Additionally, under identical exposure conditions, IFITM5$^+$ cells exhibited more fluorescence labeling of Gli1 or Prrx1 than IFITM5$^-$ cells, suggesting that IFITM5$^+$ cells also highly expressed other hallmarkers of SSCs compared to IFITM5$^-$ population (fig. S5, C and D). To test the self-renewal ability of IFITM5$^+$ cells, IFITM5$^+$ single cells were sorted to perform the serial colony formation assay. A single IFITM5$^+$ cell could clonally expand and be serially passaged, generating secondary and tertiary colonies (Fig. 5C). Compared with those of IFITM5$^-$ cells, the colony-formation efficiency and size were higher in IFITM5$^+$ cells (Fig. 5, D and E). Next, trilineage differentiation assay was performed in vitro on clonal cultures, and the IFITM5$^+$ cells showed stronger osteogenic but lower chondrogenic capacity than IFITM5$^-$ cells (Fig. 5, F to I). However, there was not obvious lipid droplet formation in both groups (Fig. 5, J and K). These data indicated that IFITM5$^+$ cells were oligopotent SSCs with self-renewal and osteogenic differentiation capacity.

CMSSCs processed strong regenerative capacity in mandible defect

To further test the in vivo differentiation potential of cells, IFITM5$^+$ and IFITM5$^-$ cells were transplanted into the renal subcapsular region of immunodeficient mice and rat mandibles defect region (Fig. 5L). The renal subcapsular grafts were harvested 8 weeks after transplantation. H&E staining showed that the size of IFITM5$^+$ cells grafts was obviously larger than that of IFITM5$^-$ cells grafts (Fig. 5M). Immunofluorescent staining of collagen I and II indicated that IFITM5$^+$ cells displayed stronger osteogenic differentiation potential than IFITM5$^-$ cells, and neither underwent chondrogenic differentiation (Fig. 5N). The higher expression level of OPN also indicated the better osteogenic differentiation capacity of IFITM5$^+$ cells (Fig. 5P). The grafted cells were detected against human nuclei marker Stem101, indicating that the tissue was generated by the transplanted cells (Fig. 5Q). To further evaluate their bone regenerative therapeutic potential, a critical-sized defect with a diameter of 5 mm in rat mandibles was generated. The gelatin methacrylate (GelMA) scaffolds loaded with IFITM5$^+$ or IFITM5$^-$ cells were implanted into the defective mandibles. Eight weeks after transplantation, the three-dimensional (3D) reconstruction and sagittal images of micro–computed tomography (CT) showed the IFITM5$^+$ cell group generated more bone (Fig. 5O), and the quantitative analysis confirmed the observation of reconstructed images (Fig. 5R). Furthermore, histological images of H&E staining and Masson staining also corroborated the findings of micro-CT analysis (Fig. 5S). The GelMA group showed lack of mineralized tissue within the defect, while the groups of IFITM5$^-$ cells displayed a small amount of regenerated bone located at the edges of the defect. Meanwhile, the IFITM5$^+$ cell group generated more mineralized bone tissue. Immunohistochemical results of Human nucleoli indicated that the implanted cells were still present in the bone defect and that the expression level of RUNX2 and OPN on consecutive sections was higher in the IFITM5$^+$ group, suggesting that IFITM5$^+$ cells generated more osteoblasts (Fig. 5T).

To test the potential of craniofacial IFITM5$^+$ cells in cortical bone regeneration of long bone, a monocortical defect (1.0 mm diameter) was made at the base of the mouse femoral neck according to Leucht's methods (fig. S6A) (*18*). IFITM5$^+$ cells and IFITM5$^-$ cells were transplanted into the defect. After 2 weeks, the 3D reconstruction and sagittal images of micro-CT indicated that the IFITM5$^+$ CMSCC group notably promoted the defect healing compared to the GelMA and IFITM5$^-$ groups (fig. S6B). The structural parameters including bone volume/total volume (BV/TV), trabecular thickness (Tb.Th), and trabecular separation (Tb.Sp) at defect region also showed a corresponding tendency (fig. S6C). Additionally, H&E staining histological images supported the micro-CT findings (fig. S6D). These results showed that CMSSCs had strong bone regeneration ability in both jawbone and long-bone repair, indicating a broader therapeutic potential.

To access whether the IFITM5$^-$ population had a detrimental effect, coculture experiments of IFITM5$^+$ and IFITM5$^-$ cells were performed. IFITM5$^+$ cells were cultured in 24-well plates, and either no cells or IFITM5$^-$ cells were placed in the top chamber of the transwell polystyrene plates (top: monoculture group; bottom: coculture group) (fig. S6E). After osteogenic induction, IFITM5$^+$ cells cocultured with IFITM5$^-$ cells exhibited stronger osteogenic properties in vitro compared to monoculture, hinting that IFITM5$^-$ population did not play a negative role in osteogenesis (fig. S6, F and G). Together, these data showed that IFITM5$^+$ cells had strong capacity in mandibular bone regeneration, indicating that these cells were CMSSCs responsible for cranio-maxillofacial bone development.

CMSSCs processed a stronger regenerative capacity in mandible defect compared to SSCs from long bone

Now, the iliac crest is the most popular source for autogenous bone transplant surgeries. It would be interesting to compare the self-renewal and osteogenic capacities of IFITM5$^+$ CMSCCs with those of SSCs from long bone. PDGFRA$^{low/-}$PDPN$^+$CADM1$^+$ SSCs (hereafter referred to as CADM1$^+$ SSCs) from long bone were sorted (Fig. 6A) and exhibited greater cloning formation ability than IFITM5$^+$ CMSCCs (Fig. 6, B and C). However, the osteogenic differentiation capacity of CADM1$^+$ cells was weaker than that of IFITM5$^+$ cells in vitro (Fig. 6, D to F). To further explore their regenerative performance in jawbone defect, we created a 1-mm-diameter defect model on the mouse mandibles and transplanted IFITM5$^+$ CMSCCs and CADM1$^+$ SSCs. Two weeks after transplantation, 3D reconstruction and sagittal images of micro-CT showed that the IFITM5$^+$ CMSCC group generated more trabecular bone (Fig. 6G). Quantitative analysis of BV/TV, Tb.Th, and Tb.Sp confirmed the observations of reconstruction images (Fig. 6H). Furthermore, H&E staining histological images corroborated the findings from the micro-CT (Fig. 6I). The results showed that IFITM5$^+$ population presented a better regenerative potential than long-bone SSCs.

IFITM5$^+$ cells still exist in adult mandible and exhibit powerful bone regeneration ability

As CMSSCs have been present at different GW during embryonic mandibular development, the presence of cells labeled with IFITM5 in the jawbone and their corresponding functions in adult bone remodeling were evaluated. To explore the temporal and spatial distribution of IFITM5$^+$ cells in the adult jawbone, jawbone

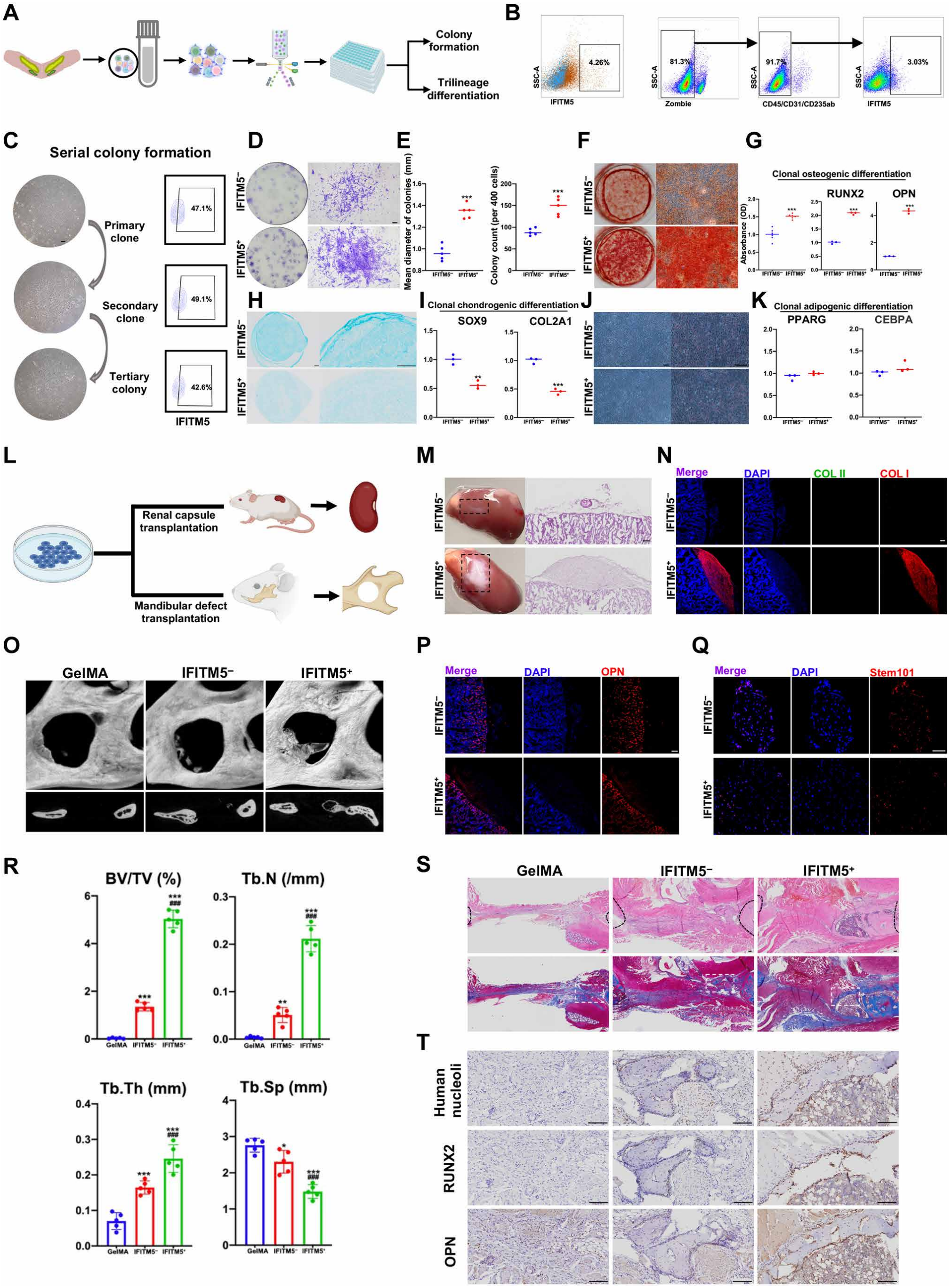

Fig. 5. Phenotypic and functional characterizations of CMSSCs. (**A**) Experimental flowchart of IFITM5$^+$ cells isolation and characterization in vitro. (**B**) Flow cytometry gating strategies for sorting IFITM5$^+$ cells ($n = 3$ embryos). (**C**) Flow cytometry plots showing serial colony formation from a single IFITM5$^+$ cell ($n = 3$ clones). (**D**) Representative crystal violet staining of fibroblast colony-forming unit (CFU-F) colonies from IFITM5$^-$ and IFITM5$^+$ cells. (**E**) Numbers and mean diameters of CFU-F colonies ($n = 3$ embryos). (**F**, **H**, and **J**) Representative alizarin red, alcian blue, and oil red O stainings after in vitro differentiation of clonally expanded IFITM5$^-$ and IFITM5$^+$ cells. (**G**, **I**, and **K**) qPCR analyses of osteogenic, chondrogenic, and adipogenic marker genes and quantification of alizarin red in clonally expanded IFITM5$^-$ and IFITM5$^+$ cells after in vitro differentiation ($n = 3$ embryos). (**L**) Workflow of IFITM5$^+$ cell characterization in vivo. (**M**) Bright-field images and H&E staining of subcapsular xenografts of IFITM5$^-$ and IFITM5$^+$ cells ($n = 5$). (**N**, **P**, and **Q**) Immunofluorescence staining of COLII, COLI, OPN, and Stem101. (**O**) Micro–computed tomography (CT) three-dimensional (3D) reconstruction images (top) and coronal images (bottom) of mandibular defect repair after GelMA, IFITM5$^-$, and IFITM5$^+$ cell transplantation. (**R**) Quantification of bone formation parameters at defect region ($n = 5$). (**S**) H&E staining (bone defect edge demarcated by black dashed lines) and Masson staining in coronal sections of GelMA, IFITM5$^-$, and IFITM5$^+$ cell groups. (**T**) Immunohistochemical staining for human nucleoli, RUNX2, and OPN in areas marked by white dashed lines in Masson staining images. Scale bars, 100 μm in all figures. [(E), (G), (I), and (K)] $**P < 0.01$ and $***P < 0.001$ determined by an unpaired two-tailed Student's *t* test. (R) $*P < 0.05$, $**P < 0.01$, and $***P < 0.001$ versus GelMA; $\#\#\#P < 0.001$ versus IFITM5$^-$ cells determined by one-way analysis of variance (ANOVA) with Tukey's post hoc test. SSC-A, side scatter-area; OD, optical density.

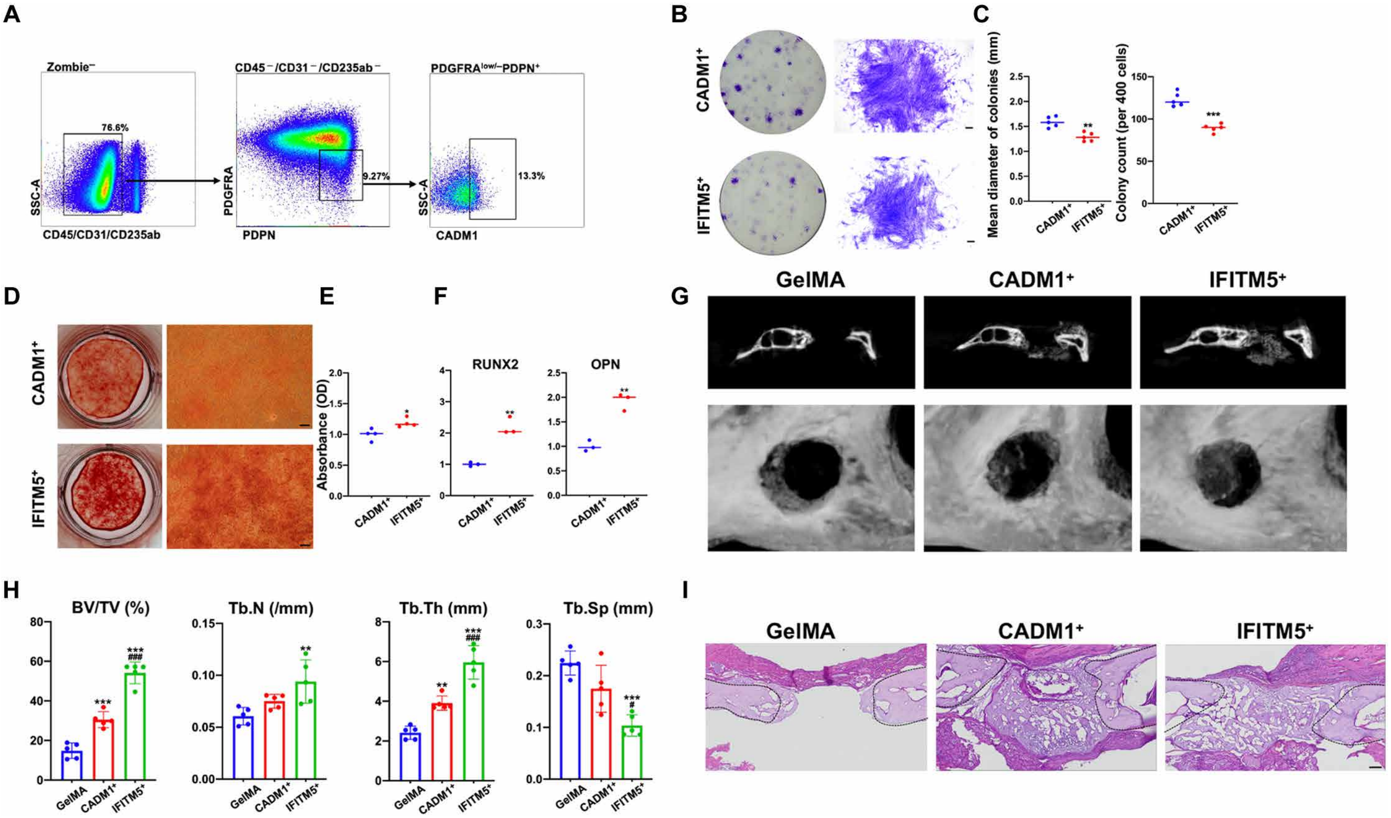

Fig. 6. Evaluation of self-renewal and osteogenic capacities of IFITM5$^+$ cells and CADM1$^+$ cells. (**A**) Flow cytometry gating strategies for sorting CADM1$^+$ cells ($n = 2$ embryos). (**B**) Representative crystal violet staining of CFU-F colonies from CADM1$^+$ and IFITM5$^+$ cells. Scale bars, 100 μm. (**C**) Numbers and mean diameters of the CFU-F colonies ($n = 2$ embryos). (**D**) Representative alizarin red staining after osteogenic differentiation of CADM1$^+$ and IFITM5$^+$ cells. Scale bars, 100 μm. (**E**) Quantification of alizarin red staining in CADM1$^+$ and IFITM5$^+$ cells after in vitro differentiation ($n = 2$ embryos). (**F**) qPCR analyses of osteogenic marker genes in vitro differentiation ($n = 2$ embryos). (**G**) Micro-CT coronal images (top) and 3D reconstruction images (bottom) of mouse mandibular defect repair after transplantation of CADM1$^+$ and IFITM5$^+$ cells. (**H**) Quantification of bone formation parameters at defect region ($n = 5$). (**I**) Representative images of H&E staining (bone defect edge demarcated by black dashed lines) in coronal sections of GelMA, CADM1$^+$, and IFITM5$^+$ cell groups. Scale bar, 100 μm. [(C), (E), and (F)] $^*P < 0.05$, $^{**}P < 0.01$, and $^{***}P < 0.001$ determined by an unpaired two-tailed Student's *t* test. (H) $^{**}P < 0.01$ and $^{***}P < 0.001$ versus GelMA; $\#P < 0.05$ and $\#\#\#P < 0.001$ versus CADM1$^+$ cells determined by one-way ANOVA with Tukey's post hoc test.

fragments from patients with maxillofacial fractures or orthognathic surgery aged 19 to 49 years were collected (Fig. 7A). Immunofluorescence analysis showed that IFITM5$^+$ cells persisted in the jawbone among patients aged 19, 32, and 49 years and were colocalized with RUNX2. The mature osteocytes embedded within the calcified matrix were unmarked by IFITM5 (Fig. 7B). The spatial distribution of IFITM5$^+$ cells overlapped with that of NG2$^+$ cells, which were considered as the marker of pericyte and often used to indicate mesenchymal stem cells in the bone marrow (fig. S7A). Next, the BMSCs were cultured from bone fragments. The primary BMSCs exhibited a typical spindle shape of a single-cell and the whirlpool arrangement type of colonies with high expression of CD90, CD105, and CD44 but lack of expression of CD34, CD45, and CD11b. The IFITM5$^+$ cells accounted for 6.52% of the primary BMSCs (Fig. 7C). Then, Zombie$^-$IFITM5$^+$ cells and Zombie$^-$IFITM5$^-$ cells were sorted from BMSCs for functional analysis (Fig. 7D). The IFITM5$^+$ and IFITM5$^-$ BMSCs both showed the high expression of CD90, CD105, and CD44 but lack of expression of CD34, CD45, and CD11b (fig. S7, B and C). IFITM5$^+$ cells generated a greater number of colonies and much larger colonies than IFITM5$^-$ cells (Fig. 7, E and F). Similarly, the IFITM5$^+$ BMSCs showed a stronger osteogenic but weaker chondrogenic differentiation capability (Fig. 7, G to K). Unlike IFITM5$^+$ cells isolated from embryonic mandible tissues, IFITM5$^+$ BMSCs exhibited a greater adipogenic potential (Fig. 7, L to N), which was accordance with the fact that adult jawbone marrow contained the adipogenic progenitor cell subset, while embryonic bone mandible tissues did not contain adipogenic cells (*32*).

Following the method mentioned above, IFITM5$^+$ BMSCs and IFITM5$^-$ BMSCs were transplanted into the renal subcapsular area and mandible defect area. After 8 weeks, the kidneys and mandibles were harvested and sectioned. A mineralization-like structure was observed in the subcapsular grafts of the IFITM5$^+$ BMSC groups, whereas only a fiber-like structure was formed in the IFITM5$^-$ BMSC groups (Fig. 7O). Immunofluorescent staining of collagen I and II revealed that IFITM5$^+$ BMSCs had strong potency toward osteogenic differentiation but not chondrogenic differentiation (Fig. 7P). The higher expression level of OPN also indicated the better osteogenic differentiation capacity of IFITM5$^+$ BMSCs (Fig. 7Q). The grafted cells were determined by Stem101 (Fig. 7R). In addition,

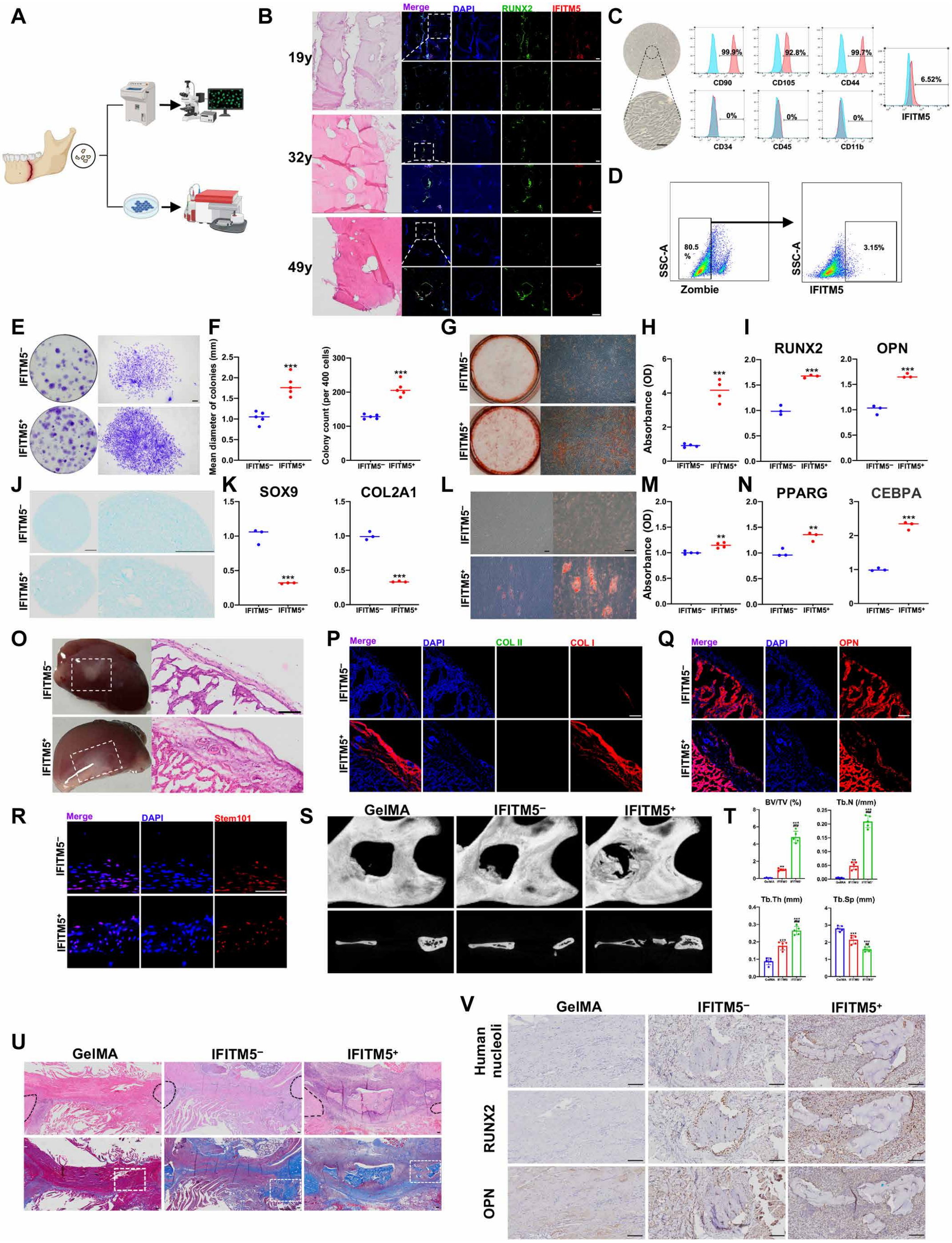

Fig. 7. Detection and functional validation of IFITM5$^+$ cells in the adult mandible. (**A**) Schematic diagram of characterization IFITM5$^+$ cells in vivo and in vitro. (**B**) H&E and immunofluorescence staining of IFITM5 and RUNX2 in mandible fragments aged 19, 32, and 49 (white boxes indicating magnified regions). y, years. (**C**) Flow analysis with MSC-specific surface markers and morphology of BMSCs ($n = 3$). (**D**) Gating scheme for sorting Zombie$^-$IFITM5$^+$ BMSCs ($n = 3$ patients). (**E**) Crystal violet staining of CFU-F colonies from IFITM5$^-$ and IFITM5$^+$ BMSCs. (**F**) Numbers and mean diameters of CFU-F colonies ($n = 3$ patients). (**G**, **J**, and **L**) Alizarin red, alcian blue, and oil red O stainings after in vitro differentiation. (**H** and **M**) Quantification of alizarin red and oil red O stainings. (**I**, **K**, and **N**) qPCR analyses of osteogenic, chondrogenic, and adipogenic marker genes ($n = 3$ patients). (**O**) Bright-field images and H&E staining of subcapsular xenografts of IFITM5$^-$ and IFITM5$^+$ BMSCs ($n = 5$). (**P**, **Q**, and **R**) Immunofluorescence staining images of COLII, COLI, OPN, and Stem101. (**S**) Micro-CT 3D reconstruction images and coronal images of mandibular defect after GelMA, IFITM5$^-$, and IFITM5$^+$ BMSC transplantation. (**T**) Quantification of bone formation parameters at defect region ($n = 5$). (**U**) H&E staining (bone defect edge demarcated by black dashed lines) and Masson staining in coronal sections of GelMA, IFITM5$^-$, and IFITM5$^+$ BMSC groups. (**V**) Immunohistochemical staining for Human nucleoli, RUNX2, and OPN in areas marked by white dashed lines in Masson staining images. Scale bars, 100 μm in all figures. [(F), (H), (I), (K), (M), and (N)] $^{**}P < 0.01$ and $^{***}P < 0.001$ determined by an unpaired two-tailed Student's *t* test. (T) $^{**}P < 0.01$ and $^{***}P < 0.001$ versus GelMA; ##$P < 0.01$ and ###$P < 0.001$ versus IFITM5$^-$ cells determined by one-way ANOVA with Tukey's post hoc test.

in the mandible defect model, a new bone in the middle area of the defect was evidently observed in the IFITM5$^+$ cell group (Fig. 7S). Quantitative analysis revealed that the amount of mineralized tissue in the IFITM5$^+$ cell group was higher than that in IFITM5$^-$ BMSCs and control group (Fig. 7T). The results of micro-CT were also verified using H&E, Masson, Human nucleoli, RUNX2, and OPN immunohistochemical staining (Fig. 7, U and V). Overall, IFITM5$^+$ cells still existed in the adult jawbone, which had robust potency of osteogenesis for bone repair and regeneration.

DISCUSSION

Recent scRNA-seq and flow sorting studies have elucidated the cellular lineage hierarchy during different bone development stages and identified multiple skeletal stem/progenitor cell populations, including CX43$^+$FGFR2$^+$ cells in deer antler blastema (*33*), CD51$^+$Thy1$^-$6C3$^-$CD105$^-$CD200$^+$ cells in mouse long bone (*14*), PDPN$^+$CD146$^-$CD73$^+$CD164$^+$ cells in human fetal growth plate (*15*), and PDGFRA$^{low/-}$PDPN$^+$CADM1$^+$ cells in the human embryonic long bone and calvarial bone (*16*). These findings demonstrated that spatiotemporal-specific subpopulations resided in different skeletal tissues in various species. The heterogeneity of postmigratory CNCCs has been well established in the mouse mandible (*8*). The spatial localization and environmental interaction of postmigratory CNCCs regulated their fate determination (*23*). However, the role of CNC-derived mesenchymal cells in human early craniomaxillofacial development has not been previously elucidated. This study generated a transcriptional landscape of human embryonic mandibles from GW8 to GW11 and identified CMSSCs, exhibiting potent osteogenic differentiation potential during intramembranous ossification, providing a cellular basis for understanding jawbone osteogenesis.

A crucial point in resolving mandibular osteogenesis is tracing the cell differentiation trajectories and spatially locating functional subpopulations. Similar to the E12.5 mouse mandible, the pseudotime analysis of scRNA-seq data revealed that common progenitors flowed toward three lineage commitments: chondrogenic lineages, osteogenic lineages, and odontogenic lineages. Combined with LCM-seq, the CMSSCs were accurately projected into osteogenic cells, and *IFITM5* was highly expressed in the osteogenic lineage of scRNA-seq. Similar to human embryonic perichondrial SSCs, the IFITM5$^+$ population could serially generate colony-forming units from single cells and undergo osteogenic differentiation but not adipogenic differentiation in vitro, suggesting that adipogenic signals had not yet been activated in the early mandible. Upon subrenal transplantation in mice, the IFITM5$^+$ population produced vast amount of collagen type I but not collagen type II, highlighting its role in mediating intramembranous ossification. These characteristics were consistent with those of Ctsk$^+$ cells from mouse long bone mediating intramembranous bone formation without cartilage formation (*28*). Thus, IFITM5$^+$ CMSSCs are oligopotent stem cells that mainly differentiate into osteogenic progenitors for intramembranous ossification.

A previous mouse study revealed that the *Ifitm5* transcripts were detectable in the mandible and the perichondrium of long bone at E14.5 when perichondrial osteoprogenitors started to differentiate into osteoblasts and form mineralized tissues (*34*). Our results showed that IFITM5 protein was detected in the periosteum of frontal bone, maxilla, and mandible at GW9, but was not expressed in the perichondrium of human long bone, vertebra, and ribs at the same stage, suggesting that the location of IFITM5 expression varied between humans and rodents. This is supported by the fact that the identified human SSCs and mouse SSCs in long bone have distinct surface markers. Clinically, patients with osteogenesis imperfecta V, caused by the c.-14C>T variant in the *IFITM5* gene, exhibit long-bone defect, suggesting that *IFITM5* is expressed at some point in human long bone (*35*). IFITM5$^+$ CMSSCs exhibited stronger bone regenerative potential in both the jawbone and long bone. Compared to long-bone CADM1$^+$ SSCs, they also had a better osteogenic effect in the jawbone. These results expanded the application field of IFITM5$^+$ CMSSCs for bone healing therapies and highlighted their powerful regeneration efficiency.

Ifitm5 was highly expressed at the early stage of mineralization in the mouse skeleton (*36*). The overexpression of *Ifitm5* promoted the mineralization of mouse osteoblasts, whereas the knockdown of *Ifitm5* inhibited the mineralization. This suggests that *Ifitm5* functions as a positive regulator of bone formation in vitro (*24*). The heterozygous *Ifitm5* c.-14C>T mutant mice exhibited perinatal lethality and strong skeletal aberrations in the craniofacial bones and long bones. This phenomenon indicated that *Ifitm5* is necessary for osteogenesis (*37*). However, in vivo studies on mice with wild-type *Ifitm5* overexpression and knockout reported that the physiological bone parameters were not altered in both neonate and adult mouse bones. Thus, *Ifitm5* is dispensable for bone development and homeostasis in mice (*38*). This study hypothesized that *Ifitm5* is an indicator of osteogenesis-related subpopulation, rather than a regulator, that plays a direct role in bone development and remodeling. Further validation using human samples is necessary to confirm the biological role of IFITM5 in bone formation.

Cranial suture SSCs, including Gli1$^+$ cells, Axin2$^+$ cells, and Prrx1$^+$ cells, were characterized by self-renewal capacity and gave rise to surrounding bone tissues (*29*, *39*, *40*). These SSCs were mainly located in the sutures of the parietal bone of the skull. In contrast to the frontal bone that originated from CNCCs derived from ectodermal mesenchyme, the parietal bone originated from mesoblast cells. Although the previous studies did not identify the origin of the suture SSCs, we speculated that these cells originating from mesoblast were distinct from the IFITM5$^+$ CMSSCs reported in this study. It is interesting to compare the molecular signatures and functions the two types of SSCs in the cranial bone.

CMSSCs from embryos exhibited a robust bone regeneration capacity. However, embryonic CMSSCs were not considered seed cells for tissue regeneration because of limited resources and ethical debates. This study demonstrated the presence of IFITM5$^+$ cells in the jawbone of adults. Adult IFITM5$^+$ BMSCs exhibited strong osteogenic and adipogenic differentiation abilities in vitro, which was consistent with the histological characteristics of the adult mandible that contained fat tissue. It is interesting to analyze the differences at transcriptome and proteome of IFITM5$^+$ cells derived from embryonic and adult tissues.

Compared with those from long bone or iliac crest, BMSCs from the jawbone showed stronger osteogenic differentiation potential in humans, rats, mice, and pigs (*41*–*44*), hinting that BMSCs from craniofacial bones were more potent for this purpose. In this study, the adult jawbone IFITM5$^+$ BMSCs had excellent bone repair ability, which could be an ideal cell type for cell-based cranio-maxillofacial bone therapy. Furthermore, BMSC-mediated bone regeneration is accompanied by the local release of several paracrine substances to mediate inflammatory responses and stimulate endogenous stem cells (*45*). The paracrine effect of IFITM5$^+$ BMSCs will be examined in future studies to understand their regenerative mechanism and optimize their application in bone regeneration.

There are several limitations in this study that warrant further investigation. First, seven lineages of mandibular mesenchymal cells were identified using scRNA-seq. However, only MCCs and CMSSCs were defined by LCM-seq analysis. In the following experiments, we will combine spatial transcriptomics to analyze the spatiotemporal evolution and communication of each lineage, providing a more comprehensive insight into human mandibular development. Second, we could not transplant uncultured IFITM5$^+$ cells because of the limited number of cells obtained from the embryonic mandible. Optimized transplantation protocol is needed to further dissect the functions of primary IFITM5$^+$ cells in vivo. Third, we only obtained distribution of CMSSCs at early stage of human embryonic mandible development and could not track the distribution of CMSSCs and their progeny over the entire development process until adulthood. Further studies using *Cre*-based lineage tracing in animal models can provide more information on the fate decision of IFITM5$^+$ cells in bone tissues.

In conclusion, this study delineated the cellular atlas of human embryonic mandibles and identified a specific IFITM5$^+$ CMSSCs during early intramembranous ossification. IFITM5$^+$ CMSSCs exhibited strong self-renewal, osteogenic differentiation, and bone defect healing capabilities. Moreover, the IFITM5$^+$ cells were detected in the adult mandibles, behaving the similar properties of bone-tissue repair. These findings improved our understanding of the early human mandibular development and provided new alternative stem cells to promote bone regeneration and treat skeletal diseases, including fracture and degenerative skeletal diseases.

MATERIALS AND METHODS

Study design

This study was performed to delineate cellular heterogeneity and lineage trajectories during human embryonic mandible development and further identified the SSCs of human cranio-maxillofacial skeleton, which broadened our understanding of the development of cranio-maxillofacial bone and provided SSCs therapies for bone regeneration. For this, we described a single-cell atlas of the human embryonic mandible by scRNA-seq and identified IFITM5$^+$ CMSSCs mediating intramembrane osteogenesis by combination with LCM. Subsequently, we explored the distribution of IFITM5 on different bone tissue and examined the function of IFITM5$^+$ CMSSCs in vitro and in vivo. In addition, we explored whether IFITM5$^+$ cells existed in adult jawbones and investigated their ability in bone defect repair.

Functional studies were performed in vivo using mouse models and in vitro using cell culture models to determine whether IFITM5$^+$ cells were a potential therapeutic candidate for cell-based bone regeneration. For all cell and animal studies, subjects were assigned randomly to groups. The parameters and sample sizes (*n*) for both in vivo and in vitro experiments were determined according to related published papers and preliminary experiments. Animal or sample allocation and data acquisition were performed in a blinded manner. No data were excluded from analyses. The number of experimental replicates for each experiment was reported in the figure legends.

Human embryonic sample collection

Healthy human embryos and fetuses were obtained with elective medical termination of pregnancy at the West China Second University Hospital. All human experimental protocols were approved by the Ethic Committee of the West China Second University Hospital (2022-307), and all studies were performed in accordance with the approved guidelines. All donors signed written informed consents and were informed about the purpose of the research. The embryos and fetuses were considered structurally normal under ultrasound examination. Detailed sample information was appended to table S1 with GW calculated from the first day of the woman's last menstrual cycle to the sample collecting date.

Animals

All animal experiment protocols and procedures were conducted in accordance with those approved by the Ethics Committee of West China Hospital of Stomatology, Sichuan University (WCHSIRB-D-2023-642). Eight-week-old NCG-immunodeficient mice (NOD/*-ShiLtJGpt-Prkdc*$^{\mathrm{em26Cd52}}$*Il2rg*$^{\mathrm{em26Cd22}}$/Gpt) were purchased from the GemPharmatech (Nanjing, China). Eight-week-old Sprague-Dawley rats and eight-week-old C57/BL6 mice were obtained from DaShuo company (Chengdu, China). All the animals were housed in specific pathogen–free conditions at Sichuan University.

BMSC cultures

Bone fragments were obtained from 19- to 49-year-old patients with maxillofacial fractures or orthognathic surgery, whose fragments could not be anatomically reducted for clinical reasons. All experiments were conducted in accordance with the ethical protocol approved by the Committee of Ethics of the West China Hospital of Stomatology, Sichuan University (WCHSIRB-D-2023-441), and informed written consents were obtained from all patients. Bone marrow was flushed out using a syringe filled with α–minimum essential medium (α-MEM). The collected flush was centrifuged at 1000 rpm for 5 min, and the precipitates were resuspended in culture medium [α-MEM, 10% fetal bovine serum (FBS), and 1% penicillin-streptomycin] in a 10-cm dish. The cell culture medium was replaced every 48 to 72 hours. The cells were passaged when cell confluence reached about 80%, and cells at passages 4 to 6 were used.

Preparation of single-cell suspensions

Human embryonic mandibles were isolated under a microscope and then washed by Dulbecco's phosphate-buffered saline (DPBS) (Servicebio, G4200) supplemented with 2% FBS (Gibco, 2364717) and 1% penicillin-streptomycin (Solarbio, P1400) on ice. The tissues were mechanically chopped into small pieces at room temperature (RT) in a digestion buffer consisting of phosphate-buffered saline (PBS) supplemented with Liberase (250 μg/ml; Roche, 5401119001) and deoxyribonuclease (200 μg/ml; Solarbio, D8071) and then incubated on a shaker at 37°C for 50 min. Digestion was terminated by adding α-MEM (Gibco, 12571063) containing 10% FBS. The digested tissues were filtered through 70-μm cell strainers (Miltenyi, 130-110-916), spun down, and resuspended in red blood cell lysis buffer (Miltenyi, 130-095-823) for 7 min. Dead cells were subsequently removed by the Dead Cell Removal Kit (Miltenyi, 130-090-101). The cells were washed twice with sorting buffer (DPBS containing 2% FBS) and resuspended at a concentration of 1×10^3 cells/μl in DPBS, followed by filtration through 30-μm cell strainers (Miltenyi, 130-110-915). Dissociation quality and cell viability were evaluated by trypan blue staining (Thermo Fisher Scientific, 15250061) and tested with a Countess II automated cell counter (Thermo Fisher Scientific, AMQAX1000) with all samples showing more than 90% viable cells. For each sample, we targeted 10,000 cells. The number of cells actually sequenced was 6148 cells for GW8, 8529 cells for GW9, 8004 cells for GW9.5, 8675 cells for GW10, and 8020 cells for GW11. What is more, the number of median genes per cell was 3431 genes for GW8, 3827 genes for GW9, 4140 genes for GW9.5, 4025 genes for GW10, and 3806 genes for GW11.

Single-cell RNA sequencing

Single cells were obtained using a Chromium Controller (10x Genomics), and scRNA-seq library were constructed using the Chromium Single cell 3′ Reagent v2 Kits in accordance with the manufacturer's instructions (10x Genomics). After quality control, the libraries were sequenced on an Illumina NovaSeq6000 platform.

Laser capture microdissection sequencing

All experiments procedures were performed according to Chen's Protocol with minor modifications (*46*). The embryonic mandible (GW9, GW10, and GW12) was washed in cold DPBS and immediately embedded and frozen in optimal cutting temperature (OCT) compound without paraformaldehyde fixation. Sections (10 μm thick) were sliced; then mounted on ultraviolet (UV)–irradiated Molecular Machine & Industries (MMI) membrane slides (MMI, Eching, Germany, 50102); treated in 100% ethanol (30 s), 75% ethanol (2 min), and ribonuclease (RNase)–free water (1 min); and stained with cresyl violet (1 min), respectively. Then, the stained sections were dehydrated with 75 and 100% ethanol for 30 s each and air-dried for 1 to 2 min before microdissection. All reagents, solutions, and buffers were made with RNase-free water. After placed onto the objective, tissue sections were microdissected using MMI CellCut Plus system, and target regions were catapulted and collected on 0.2 ml of MMI isolation caps (MMI, Eching, Germany, 50208) with diffuser caps. As for library preparation, 50 μl of 4 M guanidine isothiocyanate solution [4 M GuSCN, 50 mM tris-HCl (pH 7.5), and 25 mM EDTA; Invitrogen, 15577-018] was added to the tube bottoms of the isolation caps, and, then, the tube was inverted and incubated at 42°C for 20 to 40 min. After being centrifuged for 30 s at 7000*g* at 4°C, the lysis buffer was transferred to the 1.5-ml microcentrifuge tube on ice and added 771 μl of precipitating buffer [150 μl of nuclease-free water, 600 μl of ethanol, 20 μl of sodium acetate (1.5 M, pH 6.5), and 1 μl of glycogen (20 mg/ml)]. The lysed samples were frozen immediately at −80°C at least 30 min. Following Peng's instructions, RNA was dissolved, denatured, and reversed. cDNA was preamplificated by HotStart PCR polymerase (KAPA Biosystems, KK2502) to reduce nonspecific products and purified by AMPure XP beads (Beckman Coulter, A63881). The purified cDNA (1 ng) was transferred into sequencing library with the Illumina Nextera XT DNA Sample Preparation Kit (Illumina, FC-131-1096), and the size distribution of cDNA library was checked on an Agilent Bioanalyzer high-sensitivity chip. Last, the qualified cDNA was sequenced on an Illumina HiSeq platform at a depth of 20 million reads per library.

Processing of scRNA-seq raw sequencing data

The scRNA-seq data were aligned and quantified using the CellRanger software (version 7.1.0) with the GRCh38 human reference genome.

Integration, reduction, and identification of differential expression genes

Raw read count was subsequently processed using Seurat R package (version 4.0.5). Cells with <200 unique molecular identifiers (UMIs) or >15% of mitochondrion-derived UMI counts were considered low quality and removed. Doublets and multiplets were filtered out using DoubletFinder (version 2.0.3). The Seurat's function "ScaleData" was used to regress cell cycle effects with cell cycle markers. Harmony (version 0.1.0) was performed to integrate five samples across individuals into a shared space by removing the batch effects while preserving biological variation. Subsequently, main cell clusters were identified with the "FindClusters" function of Seurat. Clustering was performed with the Louvain clustering algorithm embedded in Seurat, and results were visualized by the UMAP method. Differential expression genes across cell clusters were identified with the "FindAllMarkers" function of Seurat.

Pseudotemporal trajectory analysis

Pseudotime trajectories were analyzed using R package Monocle3 (version 1.0.0). The "preprocess_cds" function was used to process the data, followed by the standard "reduce_dimension" and "learn_graph" functions to generate the trajectories. The marker gene expression for each cluster was visualized with "plot_genes_in_pseudotime" function of Monocle3.

LCM-seq analysis

Quality control of raw data was performed using Fastqc, and adapters were processed using Cutadapt (version 4.3) to get clean reads. The clean reads were then mapped to the human genome (GRCh38/hg38) using hisat2 (version 2.2.0). The expression level of each gene was quantified using FeatureCounts (version 1.5.3) with the reference annotation (Homo Sapiens, GRCh38.108). In addition, gene differential expression analysis was performed by DESeq2 (version 1.42.0). The differential genes were used for enrichment analysis with ClusterProfiler (version 4.11.0).

Project LCM-seq data to scRNA-seq

First, the bulk RNA-seq data were downsampled to get pseudo–single-cell data. The pseudo–single-cell data were processed like scRNA-seq data using R package projectLSI and merged with scRNA-seq data.

Method of direct projection

Seurat4 was used to process scRNA-seq and bulk RNA-seq data separately, including normalization, selection of highly variable genes, data scaling, and principal components analysis generation. The Harmony package was then used to perform batch correction on the scRNA-seq data and bulk RNA-seq data separately. To project the bulk RNA-seq to scRNA-seq data, the scRNA-seq and bulk RNA-seq data were integrated using the FindTransferAnchors and TransferData functions in Seurat. Using the integrated data, the MapQuery function was able to project these two sets of data.

Different sites and cross-species comparative analysis

To compare the presence of CMSSCs in different human bone tissues and in mouse mandibles, we obtained four expression data matrix data (GSE143753: 8-WPC calvaria and long bone, FaceBase data Record ID 1-DTK2: E10.5 to E14.5 mouse mandibles and GW9 vertebra). We integrated cellular components (common progenitors, osteogenic cells, and chondrogenic cells) from human embryonic mandibles with the mesenchymal population from other data. To explore the expression of *IFITM5*$^+$ cells across different bone or species, we used the CCA function of Seurat to integrate the data. Clustering results were visualized using UMAP.

Flow cytometry cell sorting and analysis

For the cell sorting, mandible single-cell suspensions were prepared and incubated in sorting buffer with the following antibodies: CD31–fluorescein isothiocyanate (FITC) (BD Biosciences, 555445), CD45-FITC (BD Biosciences, 555482), CD235ab-FITC (BioLegend, 306610), and IFITM5 (Adcepta, AP11058c) for 30 min at 4°C. Cells were washed once and stained for another 20 to 30 min with Alexa Fluor 647 (Life Technologies, A32573). Long-bone single-cell suspensions incubated in sorting buffer with the following antibodies: CD31-FITC (BD Biosciences, 555445), CD45-FITC (BD Biosciences, 555482), CD235ab-FITC (BioLegend, 306610), CADM1 (MBL, CM004-A64), PDPN (BioLegend, 337029), and PDGFRA (BioLegend, 323505) for 30 min at 4°C. Stained cells were washed with sorting buffer and resuspended in DPBS with Zombie Aqua dye-BV510 (BioLegend, 423102) as a live/dead cell indicator. Single cells were sorted by CytoFLEX SRT (Beckman CytoFlex, USA). Standard gating strategies were performed to exclude debris, doublets, and dead cells with unstained cells and fluorescence minus one control as a negative control. For BMSCs, cells were detached using TrypLE (Gibco, 12604013) and sorted as mentioned above.

For the flow cytometry analysis, cells were detached and incubated with following primary antibodies: CD90 (BD Biosciences, 555595), CD105 (BD Biosciences, 561443), CD44 (Abcam, ab19622), CD146 (BD Biosciences, 550315), CD34 (BD Biosciences, 555821), CD45 (BD Biosciences, 555482), and CD11b (BD Biosciences, 557396). After washes with DPBS, flow cytometry was performed using the Accuri C6 (BD Biosciences Biosciences), and FlowJo software V10.4 was used for flow cytometry analyses.

Colony-forming units

The sorted cells were seeded in six-well plate (400 cells per well) with culture medium (α-MEM containing 10% FBS, and 1% penicillin/streptomycin solution) and incubated at 37°C with 5% CO_2. The medium was changed every 3 to 4 days until colonies with more than 50 cells were observed. Cells were fixed and stained with crystal violet (Solarbio, G1062), and cell colonies with more than 50 cells were calculated. Serial colony formation was conducted by seeding sorted cells at clonal density and serially passaged to produce the secondary and tertiary colonies.

Osteogenic, adipogenic, and chondrogenic differentiation

For osteogenic differentiation, the expanded cells from single colony were seeded in 24-well plate with osteogenic differentiation induction medium (Cyagen Biosciences, HUXMX-90021), and medium was changed every 3 days until the calcium nodules were observed under the microscope. Osteogenic potential was evaluated by alizarin red staining and quantitative polymerase chain reaction (qPCR). For adipogenic differentiation, cells were cultured with four cycles of adipogenic differentiation induction medium (Cyagen Biosciences, HUXMX-90031). The adipogenic potential was then assessed by oil red O staining and qPCR. For chondrogenic differentiation, 3×10^5 cells were pelleted and fed with a chondrogenic differentiation induction medium (Cyagen Biosciences, HUXMX-90041) for 27 days, with medium changes every 3 days. The chondrogenic potential was measured by paraffin sections of the cell pellets stained with alcian blue staining and qPCR.

Quantification of alizarin red staining and oil red O staining

Cells were fixed with 4% paraformaldehyde for 15 min and stained with alizarin red or oil red O for 45 min at RT. For quantification of alizarin red staining, the stain was solubilized with 10% cetylpyridinum chloride (Sangong Biotech, A600106) by shaking for 15 min, and the absorbance was measured at 562 nm using a microplate reader (Thermo Fisher Scientific). For quantification of oil red O staining, the stain was solubilized with isopropyl alcohol, and the absorbance was measured at 510 nm.

RNA extraction and qPCR

Total RNA was extracted with the Total RNA Isolation Kit (Vazyme, RC112) according to the manufacturer's instructions. cDNA was synthesized using HiScript III RT SuperMix (Vazyme, R323). qPCR reactions were prepared using Universal SYBR qPCR Master Mix (Vazyme, Q712) and run on a QuantStudio 6 Flex Real-Time PCR System (Life Technologies). The primer sequences used was provided in the Supplementary Materials (table S2). Glyceraldehyde-3-phosphate dehydrogenase was used as loading control, and the relative RNA expression was calculated with relative quantification method ($2^{-\Delta\Delta CT}$ method).

Rat mandible defect model

Fifteen Sprague-Dawley rats (eight-week-old males) were randomly divided into three groups: the GelMA (Engineering For Life, EFL-GM-90) group, the IFITM5$^+$ cell group, and the IFITM5$^-$ cell group. After anesthetization with 3% pentobarbital (40 mg/kg), an incision was made, and muscles were bluntly dissected to expose the mandibular body. Critical-sized defect with 5 mm diameter was made using a trephine drill before the ramus of the mandible. IFITM5$^+$ and IFITM5$^-$ cells were sorted by the previous method. After that, 50 μl of cell suspension (IFITM5$^+$ cells or IFITM5$^-$ cells were centrifuged and resuspended in 7.5% GelMA for the IFITM5$^+$ group or the IFITM5$^-$ group, 1×10^7 cells/ml) was added to the defect and cross-linked by UV light irradiation for 10 s. The mandibles were harvested 8 weeks after surgery. The cells sorted from embryos, and BMSCs were performed as described above, respectively.

Mouse mandible and femur defect model

For mandible defect model, 15 C57/BL6 mice (eight-week-old males) were randomly divided into three groups: the GelMA group, the IFITM5$^+$ cell group, and the CADM1$^+$ cell group. After anesthetization and dissection, a 1.0-mm drill hole was made using a dental drill in the exposed ramus of the mandible without damaging the root. Cell suspensions (5 μl; IFITM5$^+$ cells or CADM1$^+$ cells were centrifuged and resuspended in 7.5% GelMA for the IFITM5$^+$ group or the CADM1$^+$ group, 1×10^7 cells/ml) were added to the defect and cross-linked by UV light irradiation for 10 s. For femoral defect model, 15 C57/BL6 mice (eight-week-old males) were randomly divided into three groups: the GelMA group, the IFITM5$^+$ cell group, and the IFITM5$^-$ cell group. Likewise, a monocortical defect (1.0 mm diameter) was made at the base of the femoral neck. Cell suspensions (5 μl; IFITM5$^+$ cells or IFITM5$^-$ cells were centrifuged and resuspended in 7.5% GelMA for the IFITM5$^+$ group or the IFITM5$^-$ group, 1×10^7 cells/ml) were added to the defect and cross-linked by UV light irradiation for 10 s. The mandibles and femurs were harvested 2 weeks after surgery.

Renal capsule transplantation

Ten mice (eight-week-old males) were divided into two groups (IFITM5$^+$ and IFITM5$^-$). Briefly, the mice were anesthetized, and, then, an incision was performed in the right back of each mouse to expose the right kidney. A small pocket was made to separate the capsule from the renal parenchyma. After that, 5 μl of Matrigel (Corning, 356234) containing 5×10^5 cells for the IFITM5$^+$ or IFITM5$^-$ cells was injected into the kidney pocket. The grafts were harvested 8 weeks after transplantation. Cells sorted from embryos and BMSCs were performed as described above, respectively.

Micro-CT analysis

After 8 weeks of treatment, the rat mandibles were harvested and fixed in 4% paraformaldehyde for 48 hours and then scanned using Skyscan micro-CT (Bruker, Germany). 3D reconstructions were conducted by NRecon, and the BV/TV, Tb.Sp and trabecular bone number (Tb.N) and Tb.Th at the defect site were quantitatively analyzed by CTAn. Similarly, after 2 weeks of treatment, the mice mandibles and femurs were harvested, fixed, and scanned as above.

Histological preparation and staining

For cryosections, tissues including human jawbone (GW9 and GW10), calvarial bone (GW9), vertebra and rib (GW9), mouse mandible (E14.5 and E16.5), renal subcapsular grafts, and adult jaw fragments were fixed in 4% paraformaldehyde for 24 or 48 hours, followed by decalcification in 10% EDTA (Sangon Biotech, E671001) for another 1 to 10 weeks. After that, tissues were dehydrated in 30% sucrose at 4°C overnight, embedded in OCT, and sliced into 8-μm sections (Lecia). Sections were stained using a standard H&E (Solarbio, G1120) protocol. After repaired with the Quick Antigen Retrieval Solution (KeyGen, KGIHC005) for 5 min at RT, the frozen sections were treated with blocking buffer containing 10% donkey serum (Solarbio, SL050) and 0.3% Triton X-100 in PBS for 1 hour and then incubated overnight at 4°C with following primary antibodies: Ctsk (Santa Cruz Biotechnology, sc-48353; 1:100), Ki67 (Santa Cruz Biotechnology, sc-23900; 1:100), Gli1 (Santa Cruz Biotechnology, sc-515781; 1:100), Gremlin1 (Santa Cruz Biotechnology, sc-515877; 1:100), Dlx5 (Santa Cruz Biotechnology, sc-398150; 1:100), Prrx1 (Novus, NBP1-06067; 1:100), RUNX2 (Abcam, ab76956; 1:200), IFITM5 (Adcepta, AP11058c; 1:200), COL1A2 (Zen, 380760; 1:200), COL2A1 (Santa Cruz Biotechnology, sc-52658; 1:200), OPN (Abcam, ab63856; 1:200), OPN (Santa Cruz Biotechnology, sc-21742; 1:200), NG2 (Santa Cruz Biotechnology, sc-80003; 1:200), and Stem101 (Takara, Y40400; 1:100). After washed with PBS (three times for 5 min), the sections were stained with Alexa Fluor 488 (Invitrogen, A21202, 1:500), Alexa Fluor 555 (Invitrogen, A21422; 1:500), Alexa Fluor 555 (Invitrogen, A21432; 1:500), or Alexa Fluor 647 (Invitrogen, A31573; 1:500) for 1 hour at RT, and the nuclei were counterstained with 4′,6-diamidino-2-phenylindole (DAPI; Solarbio, C0060; 1:1000) for 5 min. Images were acquired with FV1000 Olympus confocal microscopes (Olympus).

For the paraffin section, tissues including human jawbone (GW12, GW14, and GW20) and rat mandibles were fixed, decalcified, dehydrated, embedded in paraffin, and sliced into 5-μm sections (Lecia). After dewaxed and rehydrated, the sections were performed heat-mediated antigen retrieval (tris-EDTA; Servicebio, G1206) and incubated with following primary antibodies: IFITM5 (Adcepta, AP11058c; 1:200), RUNX2 (Santa Cruz Biotechnology, sc-390351; 1:300), anti-human nucleoli (Abcam, ab190710; 1:300), and OPN (Abcam, ab63856; 1:200) at 4°C overnight. Following incubation with horseradish peroxidase–conjugated secondary antibodies and visualization in 3,3 diaminobenzidine (Gene Tech, GK600710), the images were captured with VS120 Olympus microscope (Olympus). Immunofluorescent staining was performed as described above.

Cell immunofluorescence assay

IFITM5$^+$ and IFITM5$^-$ cells were seeded in 24-well plate and cultured for 24 hours. Then, cells were fixed with 4% paraformaldehyde for 30 min and incubated in 0.5% Triton X-100 for 10 min. Afterward, samples were blocked with donkey serum (Solarbio, SL050) for 1 hour before incubation overnight at 4°C with primary antibody: Gli1 (Santa Cruz Biotechnology, sc-515781; 1:100) or Prrx1 (Novus, NBP1-06067; 1:100). After washed with PBS solution three times, samples were incubated with Alexa Fluor 488 (Invitrogen, A21202; 1:500) or Alexa Fluor 555 (Invitrogen, A21432; 1:500) in a dark chamber for 1 hour and subsequently stained with DAPI (Solarbio, C0060; 1:1000) for 5 min. Stained samples were observed and pictured by an inverted fluorescent microscope (Olympus).

Statistical analysis

All the statistical analyses were performed using Prism 8.0 (GraphPad Software), and the data were shown as the means ± SD. Data were assessed with the two-tailed Student's *t* test for comparisons of two groups. One-way analysis of variance (ANOVA) with Tukey's post hoc test was used for comparisons among multiple groups. All experiments were repeated at least three times. *P* values of less than 0.05 were considered statistically significant.

Supplementary Materials

This PDF file includes:
Figs. S1 to S7
Tables S1 and S2

REFERENCES AND NOTES

1. C.-F. Chu, S.-H. Mao, V. B.-H. Shyu, C.-H. Chen, C.-T. Chen, Allogeneic bone-marrow mesenchymal stem cell with moldable cryogel for craniofacial bone regeneration. *J. Pers. Med.* **11**, 1326 (2021).
2. Z. Li, R. Ba, Z. Wang, J. Wei, Y. Zhao, W. Wu, Angiogenic potential of human bone marrow-derived mesenchymal stem cells in chondrocyte brick-enriched constructs promoted stable regeneration of craniofacial cartilage. *Stem Cells Transl. Med.* **6**, 601–612 (2017).
3. L. Mariani, X. Guo, N. A. Menezes, A. M. Drozd, S. D. Cakal, Q. Wang, E. Ferretti, A TALE/HOX code unlocks WNT signalling response towards paraxial mesoderm. *Nat. Commun.* **12**, 5136 (2021).
4. V. Lefebvre, P. Bhattaram, Vertebrate skeletogenesis. *Curr. Top. Dev. Biol.* **90**, 291–317 (2010).
5. B. R. Olsen, A. M. Reginato, W. Wang, Bone development. *Annu. Rev. Cell Dev. Biol.* **16**, 191–220 (2000).
6. J. Sun, M. Ishii, M. C. Ting, R. Maxson, Foxc1 controls the growth of the murine frontal bone rudiment by direct regulation of a Bmp response threshold of Msx2. *Development* **140**, 1034–1044 (2013).
7. Y. Chai, R. E. Maxson Jr., Recent advances in craniofacial morphogenesis. *Dev. Dyn.* **235**, 2353–2375 (2006).
8. R. Soldatov, M. Kaucka, M. E. Kastriti, J. Petersen, T. Chontorotzea, L. Englmaier, N. Akkuratova, Y. Yang, M. Haring, V. Dyachuk, C. Bock, M. Farlik, M. L. Piacentino, F. Boismoreau, M. M. Hilscher, C. Yokota, X. Qian, M. Nilsson, M. E. Bronner, L. Croci, W. Y. Hsiao, D. A. Guertin, J. F. Brunet, G. G. Consalez, P. Ernfors, K. Fried, P. V. Kharchenko, I. Adameyko, Spatiotemporal structure of cell fate decisions in murine neural crest. *Science* **364**, eaas9536 (2019).

9. C. Rolian, Endochondral ossification and the evolution of limb proportions. *Wiley Interdiscip. Rev. Dev. Biol.* **9**, e373 (2020).
10. F. Long, D. M. Ornitz, Development of the endochondral skeleton. *Cold Spring Harb. Perspect. Biol.* **5**, a008334 (2013).
11. C. Parada, Y. Chai, Mandible and tongue development. *Curr. Top. Dev. Biol.* **115**, 31–58 (2015).
12. Y. Yuan, Y. Chai, Regulatory mechanisms of jaw bone and tooth development. *Curr. Top. Dev. Biol.* **133**, 91–118 (2019).
13. P. Bianco, P. G. Robey, Skeletal stem cells. *Development* **142**, 1023–1027 (2015).
14. C. K. F. Chan, E. Y. Seo, J. Y. Chen, D. Lo, A. McArdle, R. Sinha, R. Tevlin, J. Seita, J. Vincent-Tompkins, T. Wearda, W.-J. Lu, K. Senarath-Yapa, M. T. Chung, O. Marecic, M. Tran, K. S. Yan, R. Upton, G. G. Walmsley, A. S. Lee, D. Sahoo, C. J. Kuo, I. L. Weissman, M. T. Longaker, Identification and specification of the mouse skeletal stem cell. *Cell* **160**, 285–298 (2015).
15. C. K. F. Chan, G. S. Gulati, R. Sinha, J. V. Tompkins, M. Lopez, A. C. Carter, R. C. Ransom, A. Reinisch, T. Wearda, M. Murphy, R. E. Brewer, L. S. Koepke, O. Marecic, A. Manjunath, E. Y. Seo, T. Leavitt, W.-J. Lu, A. Nguyen, S. D. Conley, A. Salhotra, T. H. Ambrosi, M. R. Borrelli, T. Siebel, K. Chan, K. Schallmoser, J. Seita, D. Sahoo, H. Goodnough, J. Bishop, M. Gardner, R. Majeti, D. C. Wan, S. Goodman, I. L. Weissman, H. Y. Chang, M. T. Longaker, Identification of the human skeletal stem cell. *Cell* **175**, 43–56.e21 (2018).
16. J. He, J. Yan, J. Wang, L. Zhao, Q. Xin, Y. Zeng, Y. Sun, H. Zhang, Z. Bai, Z. Li, Y. Ni, Y. Gong, Y. Li, H. He, Z. Bian, Y. Lan, C. Ma, L. Bian, H. Zhu, B. Liu, R. Yue, Dissecting human embryonic skeletal stem cell ontogeny by single-cell transcriptomic and functional analyses. *Cell Res.* **31**, 742–757 (2021).
17. H. S. Shu, Y. L. Liu, X. T. Tang, X. S. Zhang, B. Zhou, W. Zou, B. O. Zhou, Tracing the skeletal progenitor transition during postnatal bone formation. *Cell Stem Cell* **28**, 2122–2136.e3 (2021).
18. P. Leucht, J. B. Kim, R. Amasha, A. W. James, S. Girod, J. A. Helms, Embryonic origin and Hox status determine progenitor cell fate during adult bone regeneration. *Development* **135**, 2845–2854 (2008).
19. H. Zhao, Y. Chai, Stem cells in teeth and craniofacial bones. *J. Dent. Res.* **94**, 1495–1501 (2015).
20. Y. Weng, H. Wang, D. Wu, S. Xu, X. Chen, J. Huang, Y. Feng, L. Li, Z. Wang, A novel lineage of osteoprogenitor cells with dual epithelial and mesenchymal properties govern maxillofacial bone homeostasis and regeneration after MSFL. *Cell Res.* **32**, 814–830 (2022).
21. Y. Ding, C. Mo, J. Geng, J. Li, Y. Sun, Identification of periosteal osteogenic progenitors in jawbone. *J. Dent. Res.* **101**, 1101–1109 (2022).
22. A. Jin, H. Xu, X. Gao, S. Sun, Y. Yang, X. Huang, X. Wang, Y. Liu, Y. Zhu, Q. Dai, Q. Bian, L. Jiang, ScRNA-seq reveals a distinct osteogenic progenitor of alveolar Bone. *J. Dent. Res.* **102**, 645–655 (2023).
23. Y. Yuan, Y. E. Loh, X. Han, J. Feng, T. V. Ho, J. He, J. Jing, K. Groff, A. Wu, Y. Chai, Spatiotemporal cellular movement and fate decisions during first pharyngeal arch morphogenesis. *Sci. Adv.* **6**, eabb0119 (2020).
24. P. Moffatt, M. H. Gaumond, P. Salois, K. Sellin, M. C. Bessette, E. Godin, P. T. de Oliveira, G. J. Atkins, A. Nanci, G. Thomas, Bril: A novel bone-specific modulator of mineralization. *J. Bone Miner. Res.* **23**, 1497–1508 (2008).
25. R. Marom, I.-W. Song, E. C. Busse, M. E. Washington, A. S. Berrier, V. C. Rossi, L. Ortinau, Y. Jeong, M.-M. Jiang, B. C. Dawson, M. Adeyeye, C. Leynes, C. D. Lietman, B. M. Stroup, D. Batkovskyte, M. Jain, Y. Chen, R. Cela, A. Castellon, A. A. Tran, I. Lorenzo, D. N. Meyers, S. Huang, A. Turner, V. Shenava, M. Wallace, E. Orwoll, D. Park, C. G. Ambrose, S. C. Nagamani, J. D. Heaney, B. H. Lee, The IFITM5 mutation in osteogenesis imperfecta type V is associated with an ERK/SOX9-dependent osteoprogenitor differentiation defect. *J. Clin. Invest.* **134**, e170369 (2024).
26. J. M. Granja, S. Klemm, L. M. McGinnis, A. S. Kathiria, A. Mezger, M. R. Corces, B. Parks, E. Gars, M. Liedtke, G. X. Y. Zheng, H. Y. Chang, R. Majeti, W. J. Greenleaf, Single-cell multiomic analysis identifies regulatory programs in mixed-phenotype acute leukemia. *Nat. Biotechnol.* **37**, 1458–1465 (2019).
27. J. Roels, A. Kuchmiy, M. De Decker, S. Strubbe, M. Lavaert, K. L. Liang, G. Leclercq, B. Vandekerckhove, F. Van Nieuwerburgh, P. Van Vlierberghe, T. Taghon, Distinct and temporary-restricted epigenetic mechanisms regulate human αβ and γδ T cell development. *Nat. Immunol.* **21**, 1280–1292 (2020).
28. S. Debnath, A. R. Yallowitz, J. McCormick, S. Lalani, T. Zhang, R. Xu, N. Li, Y. Liu, Y. S. Yang, M. Eiseman, J. H. Shim, M. Hameed, J. H. Healey, M. P. Bostrom, D. A. Landau, M. B. Greenblatt, Discovery of a periosteal stem cell mediating intramembranous bone formation. *Nature* **562**, 133–139 (2018).
29. H. Zhao, J. Feng, T. V. Ho, W. Grimes, M. Urata, Y. Chai, The suture provides a niche for mesenchymal stem cells of craniofacial bones. *Nat. Cell Biol.* **17**, 386–396 (2015).
30. D. L. Worthley, M. Churchill, J. T. Compton, Y. Tailor, M. Rao, Y. Si, D. Levin, M. G. Schwartz, A. Uygur, Y. Hayakawa, S. Gross, B. W. Renz, W. Setlik, A. N. Martinez, X. Chen, S. Nizami, H. G. Lee, H. P. Kang, J. M. Caldwell, S. Asfaha, C. B. Westphalen, T. Graham, G. Jin, K. Nagar, H. Wang, M. A. Kheirbek, A. Kolhe, J. Carpenter, M. Glaire, A. Nair, S. Renders, N. Manieri, S. Muthupalani, J. G. Fox, M. Reichert, A. S. Giraud, R. F. Schwabe, J. P. Pradere, K. Walton, A. Prakash, D. Gumucio, A. K. Rustgi, T. S. Stappenbeck, R. A. Friedman, M. D. Gershon, P. Sims, T. Grikscheit, F. Y. Lee, G. Karsenty, S. Mukherjee, T. C. Wang, Gremlin 1 identifies a skeletal stem cell with bone, cartilage, and reticular stromal potential. *Cell* **160**, 269–284 (2015).
31. T. Zhou, Y. Chen, Z. Liao, L. Zhang, D. Su, Z. Li, X. Yang, X. Ke, H. Liu, Y. Chen, R. Weng, H. Shen, C. Xu, Y. Wan, R. Xu, P. Su, Spatiotemporal characterization of human early intervertebral disc formation at single-cell resolution. *Adv. Sci.* **10**, e2206296 (2023).
32. L. Zhong, L. Yao, R. J. Tower, Y. Wei, Z. Miao, J. Park, R. Shrestha, L. Wang, W. Yu, N. Holdreith, X. Huang, Y. Zhang, W. Tong, Y. Gong, J. Ahn, K. Susztak, N. Dyment, M. Li, F. Long, C. Chen, P. Seale, L. Qin, Single cell transcriptomics identifies a unique adipose lineage cell population that regulates bone marrow environment. *eLife* **9**, e54695 (2020).
33. T. Qin, G. Zhang, Y. Zheng, S. Li, Y. Yuan, Q. Li, M. Hu, H. Si, G. Wei, X. Gao, X. Cui, B. Xia, J. Ren, K. Wang, H. Ba, Z. Liu, R. Heller, Z. Li, W. Wang, J. Huang, C. Li, Q. Qiu, A population of stem cells with strong regenerative potential discovered in deer antlers. *Science* **379**, 840–847 (2023).
34. N. Hanagata, X. Li, H. Morita, T. Takemura, J. Li, T. Minowa, Characterization of the osteoblast-specific transmembrane protein IFITM5 and analysis of IFITM5-deficient mice. *J. Bone Miner. Metab.* **29**, 279–290 (2011).
35. L. Zhytnik, K. Maasalu, B. H. Duy, A. Pashenko, S. Khmyzov, E. Reimann, E. Prans, S. Koks, A. Martson, IFITM5 pathogenic variant causes osteogenesis imperfecta V with various phenotype severity in Ukrainian and Vietnamese patients. *Hum. Genomics* **13**, 25 (2019).
36. A. Patoine, A. Husseini, B. Kasaai, M. H. Gaumond, P. Moffatt, The osteogenic cell surface marker BRIL/IFITM5 is dispensable for bone development and homeostasis in mice. *PLOS ONE* **12**, e0184568 (2017).
37. N. Hanagata, T. Takemura, K. Kamimura, T. Koda, Effect of immunosuppressants on a mouse model of osteogenesis imperfecta type V harboring a heterozygous Ifitm5 c.-14C > T mutation. *Sci. Rep.* **10**, 21197 (2020).
38. C. D. Lietman, R. Marom, E. Munivez, T. K. Bertin, M. M. Jiang, Y. Chen, B. Dawson, M. A. Weis, D. Eyre, B. Lee, A transgenic mouse model of OI type V supports a neomorphic mechanism of the IFITM5 mutation. *J. Bone Miner. Res.* **30**, 489–498 (2015).
39. T. Maruyama, J. Jeong, T. J. Sheu, W. Hsu, Stem cells of the suture mesenchyme in craniofacial bone development, repair and regeneration. *Nat. Commun.* **7**, 10526 (2016).
40. K. Wilk, S. A. Yeh, L. J. Mortensen, S. Ghaffarigarakani, C. M. Lombardo, S. H. Bassir, Z. A. Aldawood, C. P. Lin, G. Intini, Postnatal calvarial skeletal stem cells expressing PRX1 reside exclusively in the calvarial sutures and are required for bone regeneration. *Stem Cell Reports* **8**, 933–946 (2017).
41. T. L. Aghaloo, T. Chaichanasakul, O. Bezouglaia, B. Kang, R. Franco, S. M. Dry, E. Atti, S. Tetradis, Osteogenic potential of mandibular vs. long-bone marrow stromal cells. *J. Dent. Res.* **89**, 1293–1298 (2010).
42. S. O. Akintoye, T. Lam, S. Shi, J. Brahim, M. T. Collins, P. G. Robey, Skeletal site-specific characterization of orofacial and iliac crest human bone marrow stromal cells in same individuals. *Bone* **38**, 758–768 (2006).
43. T. Yamaza, G. Ren, K. Akiyama, C. Chen, Y. Shi, S. Shi, Mouse mandible contains distinctive mesenchymal stem cells. *J. Dent. Res.* **90**, 317–324 (2011).
44. B. Lloyd, B. C. Tee, C. Headley, H. Emam, S. Mallery, Z. Sun, Similarities and differences between porcine mandibular and limb bone marrow mesenchymal stem cells. *Arch. Oral Biol.* **77**, 1–11 (2017).
45. X. Fu, G. Liu, A. Halim, Y. Ju, Q. Luo, A. G. Song, Mesenchymal stem cell migration and tissue repair. *Cells* **8**, 784 (2019).
46. J. Chen, S. Suo, P. P. Tam, J.-D. J. Han, G. Peng, N. Jing, Spatial transcriptomic analysis of cryosectioned tissue samples with Geo-seq. *Nat. Protoc.* **12**, 566–580 (2017).

Acknowledgments: We thank Z. Li (Sichuan University), T. Chen (Sichuan University), and Dr. Zhi Liu (Sichuan University) for helpful advice on this project. We are grateful to R. Xu (Xiamen University) and T. Zhou (Sun Yat-sen University) for providing the ScRNA-seq data of human vertebra. We thank Y. Wen and Y. Deng (State Key Laboratory of Oral Diseases, West China Hospital of Stomatology, Sichuan University) for help in cell sorting and Y. Zhen (Sichuan University) and Hongyu Zhang (Sichuan University) for help in LCM. **Funding:** This work was supported by the National Key Research and Development Program of China (no. 2022YFA1104400), the National Natural Science Foundation of China (nos. 82071092, 32300985, and U21A20369), Sichuan Science and Technology Program (nos. 2023YFS0056 and 2022YFS0126), and the Fundamental Research Funds for the Central Universities (no. SCU2023D014). **Author contributions:** Z.W. and Y.Y. performed scRNA-seq; H.C. and K.W. performed the bioinformatics analyses; J.F., F.L., and L.M. collected clinical samples; S.Z. assisted with data analysis and interpretation; Z.W. performed cell and animal experiments with the help of M.L., J.Y., X.L., and X.Z.; Z.W. and L.L. wrote the manuscript; L.L. designed the project; L.L., H.C., and W.T. supervised the project; L.L. revised the manuscript; L.L. and W.T. acquired the funding. **Competing interests:** The authors declare that they have no competing interests. **Data and materials availability:** All data needed to evaluate the conclusions in the

paper are present in the paper and/or the Supplementary Materials. The raw sequencing datasets of scRNA-seq and LCM-seq are accessed in the NCBI SRA (BioProject IDs: PRJNA1066058 and PRJNA1065776). The previous scRNA-seq data downloaded in this study can be obtained in the NCBI GEO (accession number GSE143753) and FaceBase data (Record ID 1-DTK2).

Submitted 20 February 2024
Accepted 19 November 2024
Published 1 January 2025
10.1126/sciadv.ado7852